Electron and x-ray spectroscopy of electron-atom collisions

MUHAMMAD AFZAL CHAUDHRY

Thesis submitted to the University of Stirling for the degree of Doctor of Philosophy

Atomic Physics Laboratory

University of Stirling

Stirling

1987

ABSTRACT

Electron-ion and x-ray-ion coincidence techniques have been used to measure the relative values of double-differential cross-sections for n-fold ionization, DDCS(n+), for helium, argon, krypton and xenon atoms.

In these experiments a focussed beam of energetic electrons is crossed with a dilute beam of thermal gas atoms. The electron-atom interaction can produce ionization of the atom when the incident electron energy is greater than its ionization potential. In electron-ion coincidence experiments the electrons ejected from an atom as a result of the ionization are energy analysed in a 30° parallel plate electrostatic analyser and are detected in coincidence with the product ions which are also analysed with respect to charge by a time-of-flight(TOF) type analyser. The delay time of the ions with respect to the detected electron gives information about the charge state of the ions. From these delay time spectra true coincidences are measured for every charge state n up to n = 9 to determine (Chaudhry et al. 1986; Hippler et al. 1984b) relative values of DDCS(n+) as a function of the detected electron energy and the incident electron energy. These values have been compared with other experimental data as well as theoretical values from literature, where possible.

In x-ray-ion coincidence experiments with xenon atoms, x-rays produced as a result of the de-excitation of the ionized atoms are detected with a liquid nitrogen cooled hyperpure germanium (HPGe) detector, in coincidence with the product ions which are analysed by a TOF type analyser. The time delay of the detected ions with respect to the detected x-ray gives information about the charge states of these ions.

A Bragg type crystal x-ray spectrometer (Jitschin et al. 1984) has also been set up for high resolution x-ray spectroscopy. In this instrument collimated x-rays are specularly reflected from a plane crystal which is rotated by a micro-computer-controlled stepping motor. A constant gas flow type proportional counter with a large thin window monitors the reflected x-rays. Pulses from the proportional counter are fed to an MCA in MCS mode which is also controlled by the same micro-computer. An x-ray spectrum can be built up in the MCA giving about 10-15 times better resolution than the HPGe detector in the region of the characteristic x-rays emitted by the ionized rare gas atoms.

ACKNOWLEDGEMENTS

It gives me great pleasure to acknowledge my debt of gratitude to Professor H Kleinpoppen without whose help and guidance this work would not have been possible. It was entirely due to his encouragement that I came here and stayed to complete this research.

I am also indebted to Dr A J Duncan for his guidance and encouragement. His knowledgeable comments have always been useful.

My thanks are due to Dr J Beyer for his help and the many fruitful discussions with him. My thanks are also due to Dr H Silim for his help.

I appreciate the help of the departmental technical staff, namely Mr A J Duncan, Mr A Sherman and Mr J Weir and the staff of STSC, particularly Mr J McArthur, Mr W Thomson and Miss L North.

My study abroad would not have been possible without the help and support of my parents, my brothers Mr M Aslam Chaudhry, Dr Asgher A. Hameed and sister in law Dr N B Hameed and other members of my family and the great sacrifice of my wife and children who missed me greatly during this period.

My thanks are also due to my colleagues and friends, specially Mr M D Moughal, and Mr M A Shah for their encouragement.

Finally my thanks to Mrs H Queen for typing this manuscript so very carefully.

CONTENTS

CHAPTER 1

INTRODUCTION

CHAPTER 1

1. INTRODUCTION

The collision of an electron with an atom is in general a complex phenomenon. The interaction results in processes like elastic scattering, which dominates at low energies, excitation processes to bound and continuum states (ionization) and electron exchange processes.

The ionization of atoms by fast electrons is of importance in a number of fields such as plasma physics, radiation physics, atmospheric physics and astrophysics, and in the study of the penetration of matter by electrons (Bethe, 1930, 1933; Massey and Mohr, 1933; Fano, 1963; Inokuti, 1971). For most of these applications only total ionization data is needed. The most recent experimental values of ionization cross sections for atomic gases are those of Nagy et al. (1980) and Schram (1966). Kieffer and Dunn (1966) have made a compilation of the earlier experimental data from which it is clear that there is $\sim$ 20% disagreement between the earlier experimental values of different research groups. Two methods have been used for calculation of ionization cross sections (Nagy et al., 1980). One method is based on the sum rule which states that the difference between the total inelastic scattering cross section, $\sigma_{tot,inel}$, and the excitation cross section σ_{exc}, gives the ionization cross section σ_{ion}, (Inokuti et al., 1967; Inokuti, 1971; Saxon, 1973; Kim et al. 1973; Eggarter, 1975). The other theoretical treatment is based on the dispersion-relation analysis of electron-atom scattering (Bransden and McDowell, 1969, 1970; de Heer et al., 1979). For this analysis accurate values of the total scattering cross section, σ_{tot}, are very important (de Heer and Jansen, 1977; de Heer et al. 1979) since use is made of the relation $\sigma_{tot} = \sigma_{exc} + \sigma_{ion} + \sigma_{el}$ where σ_{el} is the total elastic scattering cross section.

For a number of applications a knowledge of the energy and angular distribution of the ionized electrons (variously referred to as ejected or secondary electrons) produced in the electron-collision process, are also necessary. In this case from a theoretical point of view the basic quantity which is calculated is a triple differential cross section (TDCS). differential in the solid angle of the scattered electron, the solid angle of the ionized electron, and the energy lost by the scattered electron. The integration of the TDCS over the scattered electron energy yields the double differential cross section (DDCS), i.e. the ionization cross section differential in energy and angular distribution of the ionized electron. A number of measurements of the DDCS have been published (Ehrhardt et al., 1972; Peterson et al. 1971, 1972; Opal et al. 1971, 1972; Vroom et al. 1977; Oda et al. 1972; Tahira and Oda, 1973; Shyn et al. 1979, 1981; Kim Y.-K. (1983). Theoretical studies of DDCS in the first Born approximation (FBA) (Madison, 1973; Bell and Kingston, 1975); plane wave Born approximation (PWBA) (Tahira and Oda, 1973, and references therein)and binary encounter theory (BET) (Oda et al. 1972; Vriens, 1969; Bonsen and Vriens, 1970) have been reported.

Another aspect of the electron-atom collision process, which is of large interest, is the multiple ionization of the atom. Electrons can produce multiple ionization via several processes:

(a) direct multiple ionization

(b)multiple ionization involving correlation between electrons,

(c) ionization of inner shells followed by Coster-Kronig and/or Auger transitions,

(d) ionization followed by a core relaxation process (shake-off).

The investigations of the multiple ionization process have employed direct detection of multiply charged ions (Van der Wiel and Wiebes, 1971); Schram, 1966; Nagy et al. 1980 or have used indirect

means such as the detection of vacuum ultraviolet radiation (Beyer et al. 1979), Auger electrons (Stolterfoht et al. 1973) or characteristic x-rays (Oona, 1974). In these studies total cross sections for the production of multiple ionization are measured.

In the present work, however, we have investigated the electron-atom collision process in more detail by measuring double differential cross sections for n-fold ionization, or partial double-differential cross sections DDCS(n+), i.e. ionization cross sections for multiple ionization differential in secondary electron energy and its ejection angle, using the electron-ion coincidence technique.

The experimental set up for measuring DDCS(n+) by the electron-ion coincidence technique is given in section 4.1. In these experiments electrons ejected at 90° to the incident electron direction are energy analysed and then detected in coincidence with product ions which are analysed by a time-of-flight (TOF) type analyser. The apparatus used in these experiments is discussed in sections 3.1 to 3.5. Relative values of the DDCS(n+) and the DDCS (obtained by summing the DDCS(n+) over all values of n) have been measured for helium, argon, krypton and xenon as a function of secondary electron energy and incident electron energy. The results have been discussed in section 5.1. Present DDCS values have been compared with other similar experimental data from literature. Comparison with theoretical predictions have also been given where possible. In the absence of a comprehensive theoretical explanation for multiple ionization (McGuire, 1982), the values of DDCS(n+) for these many-electron atoms cannot be checked against theory. For neon, a single measurement is reported in Section (5.1.5).

The experimental set up for the x-ray-ion coincidence experiment, investigating the electron-xenon-atom collision process, is given in

section 4.2. In this study x-rays are detected by a liquid nitrogen cooled hyperpure germanium (HPGe) detector while ions are analysed for charge state by a TOF type analyser. The apparatus used for this experiment is described in section 3.7. The results are discussed in section 5.2.

A plane crystal x-ray spectrometer (Harbach, 1980; Werner, 1983; Jitschin, 1984) has been used to study K_α and K_β x-ray lines emitted by ^{54}Mn as a result of electron capture (EC) in a ^{55}Fe radio-active source. The apparatus is discussed in section 3.8 and the experimental set up, including the circuit for interfacing it with a BBC microcomputer, is given in section 4.3. The results of this experiment are discussed in section 5.3.

CHAPTER 2

THEORY

2.1 Cross section for ionization of atoms by electron impact

Theoretical treatment of electron impact ionization remains a difficult problem of atomic physics, and yet there is no satisfactory procedure for describing the process (Jacobowicz & Moores, 1983) Reviews of theory are given by Rudge (1968) and Peterkop (1977). The source of the difficulties is the long-range nature of the Coulomb potential which ensures that the two continuum electrons continue to interact with the residual ion and each other until they are well apart. A complete treatment of the ionization process, therefore, requires a full solution of the three body problem in the asymptotic region. In practical calculations it is usual to make several approximations about target states, incident particle waveforms and, for simplification, to neglect correlation between continuum electrons.

Atomic ionization can be expressed in terms of various cross sections, e.g. total cross section, partial cross sections and differential cross sections of various degrees. The most complete description of an ionization is provided by determining the energy and momentum of all particles in the collision. The triple differential cross section (TDCS), in the case of single ionization under electron impact, thus defined is given by (Ehrhardt et al. 1972)

$$\frac{d^3\sigma}{dE d\Omega_A d\Omega_B} = f_3(E_o, E_A, \theta_A, \theta_B, \phi_B) \qquad 2.1\text{-}1$$

where E_o is the incident energy, E_A the energy of one of the electrons and θ_A the angle it makes with the incident electron direction while ϕ_B and θ_B define the direction of the second electron. The double differential cross section (DDCS), differential in the energy of the scattered electron and the direction of one of the outgoing electrons,

can be obtained by integrating the TDCS over the direction of one of the outgoing electrons. The integration of TDCS over the direction of both outgoing electrons yields the single differential cross section (SDCS) which is differential only in the energy or angle of the secondary electrons. Further integration of the SDCS over the energy of the secondary electrons yields total ionization cross section.

2.1.1 Double differential cross sections (DDCS) for ionization of atoms

There are several approximations available for the calculation of the DDCS for secondary electrons. The first Born approximation (Massey & Mohr 1933; Rudd et al. 1966 and Oldham Jr. 1965 and 1967; Tahira and Oda, 1973), the plane-wave Born approximation (Wetzel 1933; Glassgold and Ialongo 1968, 1969; Vriens 1970 and Cooper and Kolbenstredt 1972; Tahira and Oda, 1973; Kim and Inokuti, 1973; Bell and Kingston, 1975 and Manson et al. 1975, and the binary encounter theory (Vriens, 1969; and Bonsen, Vriens 1970; Tahira and Oda, 1973), are considered to be practical methods (Tahira and Oda 1973) for calculation of DDCS. These will be discussed here briefly.

2.1.2 First Born approximation

The TDCS for the ionization of the hydrogen atom by electron impact has been given in the first Born approximation by Massey and Mohr (1933), Mott and Massey (1965), Massey et al. (1969) and Landau and Lifschitz (1965). The DDCS in this approximation can be represented as the sum of DDCS for scattered electrons and that for ejected electrons (Tahira and Oda, 1973), where for mathematical simplicity either one of the two outgoing electrons is called "ejected" and the other is called "scattered". In fact it is not possible to differentiate

between the scattered and the ejected electron. The DDCS for ejected electrons is obtained by integrating the TDCS over the direction of scattered electrons while the DDCS for scattered electrons is calculated by integrating the TDCS over the direction of the ejected electrons. The values of the DDCS for the hydrogen atom have been calculated by Tahira and Oda, 1973. The DDCS for other atoms can be obtained from that for hydrogen atom using the scaling methods of Rudd et al. 1966, or Tahira and Oda, 1973. Bonsen and Vriens (1970) have shown, in the case of proton impact, that the scaling of hydrogenic cross sections for helium on the expectation value for the kinetic energy of the atomic electrons (39.49 eV) leads to cross section values that are in much closer agreement with the more accurate Hartree-Fock ones than the scaling on the ionization potential U(24.58 eV). The scaling procedures using 39.49 eV-value and 24.58 eV-value are equivalent to the use of $z = 1.704$ and 1.344, respectively in the scaling equations (Tahira and Oda, 1973). Here z is the effective nuclear charge.

Bell and Kingston (1975) have calculated values of the DDCS for helium by electron impact at energies between 200 eV to 2000 eV, using the first Born approximation. Their conclusions, after comparison with experimental results, are that:

(i) the Born approximation is unreliable below 200 eV incident electron energy,

(ii) at 500 eV, there is quite good agreement, and

(iii) at an incident energy of 2000 eV, the only serious disagreement between theory and experiment is in the forward scattering direction for slow ejected electrons.

2.1.3 Plane-wave Born approximation

The triple differential cross section in this approximation is given in atomic units by (Glassgold and Ialongo, 1968, 1969; and Vriens, 1970)

$$\frac{d^3\sigma}{dE d\Omega_e d\Omega_s} = \frac{4k_s k_e}{k_i} \left[\frac{1}{q^4} + \frac{1}{S^4} - \frac{1}{q^2 S^2} \right] \times$$

$$|\phi_i(\underline{k}_s + \underline{k}_e - \underline{k}_i)|^2 \delta(k_i^2 - k_s^2 - k_e^2 - 2U) \qquad 2.1.3\text{-}1$$

where S is the magnitude of the exchange momentum transfer vector, $S(= \underline{k}_i - \underline{k}_e)$, q the magnitude of the direct momentum transfer vector $\underline{q} = \underline{k}_i - \underline{k}_s$, and $\phi_i(\underline{k})$ is the initial state wave function of the target atom in momentum space. In the particular case of helium, when the hydrogenic wave function is assumed for the initial state, the expression for $|\phi_i(\underline{k})|^2$ is given by (Sneddon, 1951)

$$|\phi_i(\underline{k})|^2 = \frac{8z^5}{\pi^2} \frac{1}{(k^2 + z^2)^4} \qquad 2.1.3\text{-}2$$

The direct term of equation 2.1.3-1 is identical with that obtained by Wetzel, 1933, if one treats hydrogenic atoms and takes account of only the e^2/r_{12} term in the perturbation r_{12} being the distance between the colliding electron and the atomic electron.

When k_s is taken as the momentum of the detected electron, the DDCS is obtained by integrating $d^3\sigma/dE d\Omega_e d\Omega_s$ over the direction of k_e, and the DDCS can be written (Tahira and Oda, 1973) in units of $(a_o^2/2R_y)$ as

$$\frac{d^2\sigma}{dE_s d\Omega_s} = \frac{32z^5}{\pi^2} \frac{k_s k_e}{k_i} n[\sigma_D + \sigma_{EX} + \sigma_I] \qquad 2.1.3\text{-}3$$

where σ_D , σ_{EX} and σ_I are the direct, exchange, and interference terms,

respectively, z is the atomic number and n is the number of atomic electrons (n=2 for helium).

The expressions for σ_D , σ_{EX} and σ_I are given by Tahira and Oda (1973).

At intermediate and higher incident electron energies theoretical PWBA calculations for DDCS agree fairly well with the experimental measurements (Tahira and Oda, 1973).

Manson et al. (1975) have given calculations, for DDCS, based on the Born approximation with Hartree-Slater (HS) initial discrete and final continuum wave functions for helium. Their calculations show a good agreement with the experimental values except at 30° and 150° secondary electron ejection angles.

2.1.4 Binary encounter theory

In the binary encounter theory (BET) (Vriens, 1969) an incident electron is supposed to interact with only one of the atomic electrons at a time and the cross sections for the electron-atom collisions are obtained by integrating the cross sections for the binary encounter collisions between incident and atomic electrons over the momentum distribution of the atomic electrons. The DDCS in this approximation is given in terms either of the energy of ejected electrons E_e, or the energy of scattered electrons E_s. The direct, exchange and interference terms are taken into account.

The DDCS in terms of E_e is given in atomic units by Tahira and Oda,(1973)

$$\frac{d^2\sigma}{dE_e d\Omega_e} = n \int_{k_{min}}^{k_{max}} \left[\sigma_D(k) + \sigma_{EX}(k) - \frac{1}{2}\sigma_I(k) \right] f(k)\, d\,k \,, \qquad 2.1.4\text{-}1$$

where $\sigma_D(k)$, $\sigma_{EX}(k)$, and $\sigma_I(k)$ are the direct, exchange, and interference terms, respectively, n is the number of atomic electrons, k_{min} and k_{max} are the lower and upper bounds respectively (Bonsen and Vriens, 1970) for the momentum of atomic electrons contributing to the differential cross sections and f(k) is the momentum distribution of atomic electrons. The first term of eq. 2.1.4-1, the direct term was first formulated by Bonsen and Vriens (1970) for the case of proton impact. The second and third terms were derived by Tahira and Oda (1973).

At relatively low incident electron energies and detection angles between 30° and 90° the agreement between theoretical and experimental results is quite good (Tahira and Oda, 1973). As the BET does not include phase shift effects, it cannot be expected to represent the DDCS properly at large angles (Bonsen and Vriens, 1970).

2.1.5 Inner shell ionization

The ionization of inner shells can be effected in several ways. The expression for ionization cross section under electron impact as obtained by Mott and Massey (1965) is

$$Q_{n\ell} = \frac{2\pi e^4 Z_{n\ell}}{mv\, E_{n\ell}}\, b_{n\ell} \log_e \frac{2mv^2}{B_{n\ell}} \qquad 2.1.5\text{-}1$$

where $Q_{n\ell}$ is the cross section for the $(n\ell)$th shell, e, m, the electronic charge and mass, respectively, v the velocity of the incident electron. $b_{n\ell}$ and $B_{n\ell}$ are constants. $Z_{n\ell}$ is the number of electrons in the $n\ell$ shell. Values of 0.35 for $b_{n\ell}$ for the K shell and 1.65 $E_{n\ell}$ for B (where $E_{n\ell}$ is the ionization potential) are given by Burhop (1940). The logarithm in the equation (2.1.5-1) can be written as $\log_e(4E/1.65\ E_k)$ where E = the kinetic energy of the incident electrons and E_k is the binding energy of the K-shell. The Bethe-Bloch energy-loss equation given by Segre (1959) has the logarithm term in the form $\log_e(2E/E_k)$

and there is some uncertainty in the details of this part of the expression which is important in the region where E does not greatly exceed E_k.

Worthington and Tomlin (1956) have derived an empirical formula for $B_{n\ell}$ which approaches 1.65 E_k for large excitation voltages, but which allows $B_{n\ell}$ to approach $4E_k$ for excitation voltages just exceeding the excitation limit (U>1). Their expression for B is

$$B_{n\ell} = [1.65 + 2.35 \exp(1-U)]E_k \qquad 2.1.5\text{-}2$$

where U is the excitation ratio E/E_k. The equation 2.1.5-1 becomes

$$Q_k = \frac{2\pi e^4 b_{n\ell}}{U E_k^2} \log_e (4UE_k/B_{n\ell}), \qquad 2.1.5\text{-}3$$

This expression and the previous one shows that $Q_k E_k^2$ is the same function of U for all elements and that, $Q_k E_k^2$ for U>1, can be written in a simple form (Worthington and Tomlin, 1956)

$$Q_k E_k^2 = \frac{2\pi e^4}{U} (0.7) \log_e U \qquad 2.1.5\text{-}4$$

If E_k is expressed in electron volts this becomes

$$Q_k E_k^2 = 2\pi e^4 \frac{\log_e U}{U} \times 6.3 \times 10^4 \text{(e in e.s.u)}$$

$$= 9.12 \times 10^{-14} \frac{\log_e U}{U} \quad (\text{eV})^2 (\text{cm})^2 \qquad 2.1.5\text{-}5$$

The cross sections for the heavier elements are in fact considerably greater than those expected from equations 2.1.5-4 and 2.1.5-5. Some experimental data has been shown to be in agreement with the relativistic calculations of Arthurs and Moiseiwitch (1958). A discussion of relativistic cross-sections for K-shell ionization is given by Perlman (1960).

Hippler and Jitschin (1982) have calculated K-shell ionization cross sections for light atoms using the plane wave Born approximation (PWBA) and Ochkur approximation. Their inclusion of exchange effects has considerably improved agreement with experimental results. Use of the distorted wave Born approximation (DWBA) (Madison and Shelton, 1973) and Coulomb-exchange method (Moors et al. 1980) may resolve the remaining inadequacies (Hippler and Jitschin, 1982).

2.1.6 Auger transitions

Inner-shell vacancies in atoms decay by the emission of photons or electrons. De-excitation by photons leads to the production of characteristic x-rays while decay by the emission of an electron is called autoionization or an Auger transition depending on whether the excited state occurs in a neutral atom or in an ionized atom. An autoionizing state can be formed by excitation of an inner-shell electron to an empty but bound orbital while an Auger state is created by inner-shell ionization. In the case of neon, for example, only K-shell ionization leads to an Auger state whereas the 2S-ionization leads to an excited Ne^{+} atom, the energy of which is still below the continuum threshold of Ne^{++}, which therefore decays only by emission of a radiation. The Auger state $1s^{-1}$ decays to one of the final ionic states $2s^{-2}$, $2s^{-1}2p^{-1}$ or $2p^{-2}$ giving rise to normal or diagram Auger-transitions. Starting with more than one vacancy in the initial state, e.g. $1s^{-2}2p^{-1}$ the corresponding Auger transitions are called satellite transitions. The Auger effect was predicted by Rosseland (1923) and observed by Auger (1925). Wentzel (1927) gave a non-relativistic theory for Auger transitions which was reviewed by Burhop in 1952.

If the initial state is given by a single inner-shell vacancy and the final state just by two vacancies, the corresponding transition is called a normal or a diagram transition. If the atom, in addition to the inner vacancy, is multiply ionized in outer shells, the Auger spectrum contains only satellite lines. In the case when more than two electrons are involved in the transition, e.g. K-LLL or K-LLL* or KK-LLL, the transitions give rise to correlation satellite lines. Transitions such as K-LLL or K-LLL*, where either two electrons are ejected simultaneously (Carlson and Kraus 1965, 1966; Åberg 1975) or one electron is ejected and another electron is excited (Mehlhorn 1976), are known as double Auger transitions. In the K-LLL transition both ejected electrons share the transition energy leading to a continuous energy distribution:

$$E_{Auger_1} + E_{Auger_2} = E(K) - E(LLL).$$

In the K-LLL* transition the energy of the ejected electron is smaller than it would otherwise be by an amount equal to the excitation energy of the other excited electron and is given by

$$E_{Auger} = E(K) - E(LL) - E_{excitation}.$$

Transitions such as KK-LLL, three-electron Auger transitions in an atom with two vacancies have been found by Afrosimov (1976) and Shergin and Gordeev (1977) in heavy ion-atom collisions where the formation of two K vacancies has a much larger cross section than for electron or proton impact.

2.1.7 Coster Kronig transitions

A transition, where one of the final vacancies occur in the

same main shell but different subshell, is referred to as a Coster-Kronig (CK) transition, e.g. $L_1L_{23}M$. The energy of Coster-Kronig electrons is correspondingly smaller and in some cases Coster-Kronig transitions are forbidden. On the other hand, Coster-Kronig transitions may sometimes have a much larger transition probability ($\sim$ 10 times) than their competing Auger transitions (e.g. L_1MM).

If both final vacancies occur in the same main shell, the transitions are called super-Coster-Kronig (SCK) transitions. Because of the energy considerations, these transitions can only occur in atoms with atomic number z within a certain range (McGuire 1974, Yin 1974 and Chen et al. 1976). Their occurrence changes completely the photo-electron spectra. For example, for $Z < 54$ due to the strong decay probability of the 4p vacancy, the 4p photo-electron is completely diluted in the background and/or shifted several eV to lower energies (Wendin and Ohno (1976); Krause (1976)).

2.2 Characteristic x-rays

Characteristic x-rays can arise from the rearrangement of orbital electrons of an atom following ejection of one or more electrons in an inner-shell excitation or ionization process. When a vacancy in an inner-shell is filled, the atom changes to a state of lower energy and this excess energy may be released in two ways: either an x-ray photon may be emitted or alternatively a radiationless transition may take place in which the available energy is used to release an electron from an outer shell.

To calculate the relative intensities of lines emitted in allowed transitions we make use of the 'sum rules' which state that, for the lines comprising a multiplet, the total intensity of all lines proceeding from a common initial level or to a common final level is

proportional to the statistical weight (2J + 1) of that level. The relative intensity of some K and L series have been calculated by Beckman (1955).

The width of the lines of the characteristic x-ray spectrum has been examined as a function of atomic number and is found to exhibit several interesting features. It is well known that the energy width of a state and its lifetime are related by the Heisenberg uncertainty principle $\Gamma\tau = \hbar$ where Γ is the width in energy units and τ the mean lifetime of the state. If P is the probability per unit time of the transition time one can write $\tau = P^{-1}$ and $\Gamma = hP$. In the case of a transition from a state of inner-shell ionization, the probability of radiative and non-radiative (Auger) transitions may be written as P_r and P_n and the lifetime will thus be given by $(P_r + P_n)^{-1}$. The presence of competing processes thus reduces the lifetime of the state and must, therefore, through application of the uncertainty principle, increase the width of the state. The total width Γ_t may be defined as the sum of two partial widths Γ_r and Γ_n where $\Gamma_r = hP_r$ and $\Gamma_n = hP_n$.

2.3 Partial double-differential cross section for ionization

Double-differential cross section for n-fold ionization or partial double-differential cross section, DDCS(n+), can be approximated to

$$\text{DDCS} = \sum_n \text{DDCS(n+)} \qquad 2.3\text{-}1$$

where n is the charge state of ionization.

The values of DDCS mainly reflect the M-shell DDCS since K- and L-shell DDCS are comparatively small (Hippler, 1984c). To obtain DDCS and DDCS(n+) for K- and L-shell one has to perform a coincidence experiment between

(a) ejected electrons and Auger electrons or characteristic x-rays, or

(b) ions and Auger electrons or characteristic x-rays, following the decay of specific inner-shell vacancies, to effectively suppress the detection of ejected electrons from other shells.

The DDCS(n+) can give very useful information about multiple ionization in the collision process. Unfortunately, not much theoretical literature exists in this regard and the only experimental investigations for the measurement of DDCS(n+) are

(i) for the electron-argon atom collision process by Hippler et al., 1984b,

(ii) for proton collisions with helium, neon and argon gas atoms by Hippler et al., 1984a and

(iii) for electron-rare gas atoms by Chaudhry et al. 1986.

CHAPTER 3

APPARATUS

3.1 Vacuum Chamber Housing the Apparatus

Figure 3.1(a) shows the vacuum chamber and the apparatus housed inside. The vacuum chamber is a non-magnetic stainless steel cylinder, closed at one end, which has an outer diameter of 70cm and a length of 60cm. The chamber is mounted on a base flange, also made from non-magnetic stainless steel, and can be vacuum sealed with a viton 'O' ring. A hoist is fixed to the closed end of the chamber which enables it to be lifted, giving access to the components of the apparatus inside the chamber.

A high vacuum of the order of 2×10^{-7} torr can be maintained in the chamber with the help of an Edwards MK2 diffstak, a high vacuum pump, which uses Santovac 5 as pumping fluid and has a pumping speed of 700 litres/sec for air. An Edwards rotary oil pump acts as the backing pump for the system. There is an oil trap between the backing pump and the diffusion pump to absorb oil vapours from the backing line. In the event of failure of cooling water or power, an interlock unit actuates an air-pressure-controlled butterfly valve which isolates the vacuum chamber from the pumping system. The diffusion pump is then automatically switched off and a magnetic valve isolates the rotary oil pump from the diffusion pump.

Figure 3.1(b) shows the apparatus inside the vacuum chamber. The electron gun (right), the Faraday cup (left), the ion analyser (top) and the electron analyser (at the back) are all supported on turn-tables to facilitate their independent motion.

3.2 Electron Gun and Faraday Cup

The electron gun used in these experiments is a directly-heated tungsten filament type gun capable of producing a high energy focussed beam of electrons having a diameter of about 2mm in the interaction region. Figure 3.2(a) illustrates the gun schematically. The hairpin

Figure 3.1(a): The Vacuum Chamber

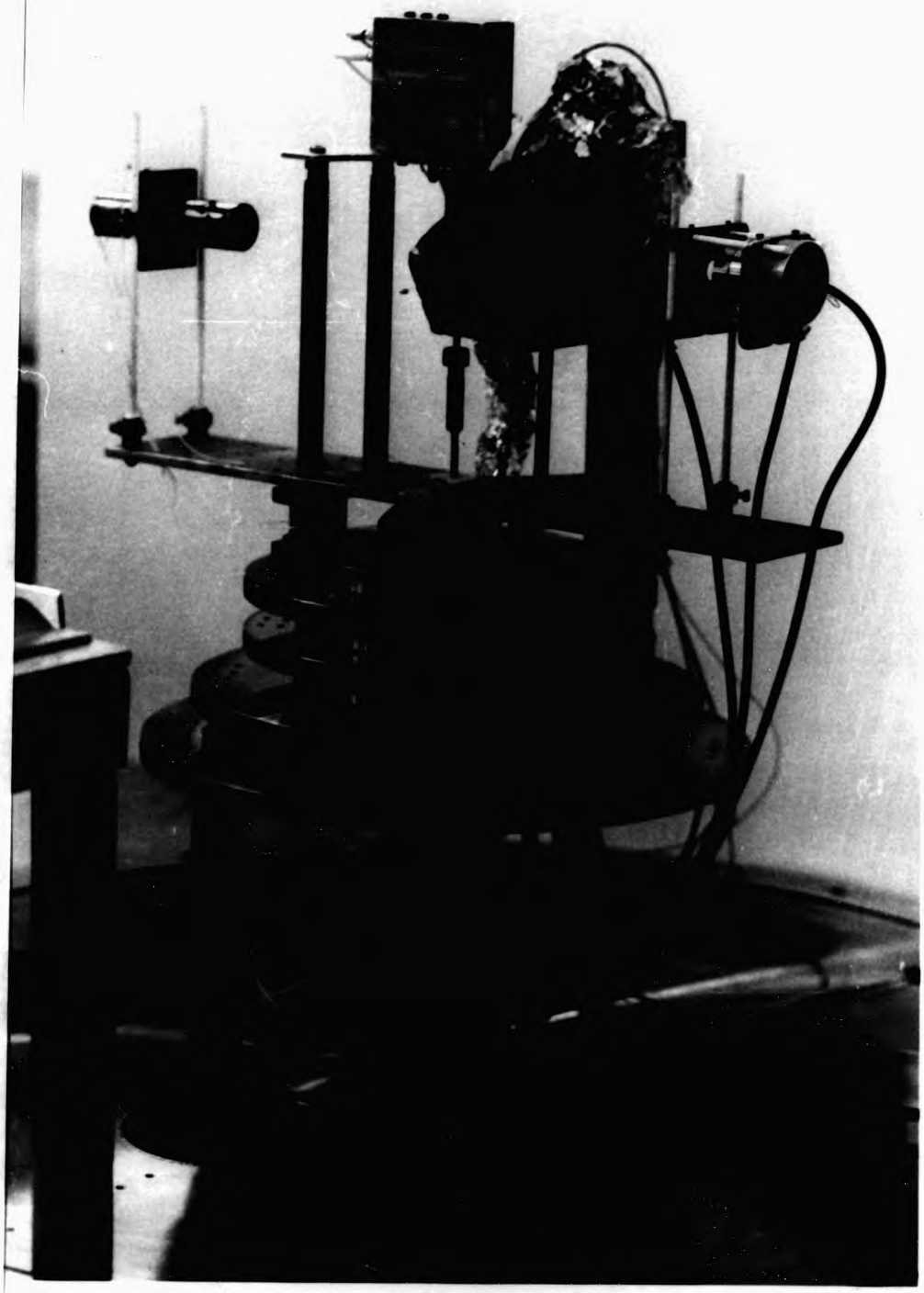

Figure 3.1(b): The apparatus inside the Vacuum Chamber

shaped tungsten filament (supplied by Agar Aids) is mounted on a ceramic support. It needs a heating current of about 2.7 amperes and can supply an electron beam current of several microamperes.

The electron gun assembly which is supported by ceramic rods is kept floating at high voltage while the voltage on the next electrode can be varied to focus the beam on the last (collimating) electrode which is kept at ground potential.

A Faraday cup collects the electron beam after its interaction with gas atoms. The Faraday cup consists of three cylinders, of varying diameters and lengths and made from aluminium, which are supported on boron nitride spacers to keep them electrically isolated from one another. Figure 3.2(b) shows the Faraday cup assembly in detail. The Faraday cup has very low back scattering and secondary emission and thus over 95% of electrons reaching the Faraday cup are collected. Kuyatt (1968), has discussed various configurations of Faraday cups suitable for preventing secondary electron emission. To further minimise secondary electron emission from different parts of the electron gun and Faraday cup, they have all been sooted. A Keithly electrometer (model 610CR) measures the electron current.

3.3 Atomic Beam Source

A well defined beam of atomic gases is obtained by effusing the gases through a nozzle consisting of a multi-capillary array (Lucas 1972). Each capillary is 3mm long and has an internal diameter of 0.05mm. The multi-capillary array is encased in a long demountable aluminium capsule which is welded to a brass tube having an inner diameter of 6 mm. This tube carrying the gas nozzle enters the vacuum chamber through the base flange along the axis of rotation of the turntables carrying the electron gun, Faraday cup and electron analyser. Gas, at low pressure, is supplied to this assembly from a pressure regulating system

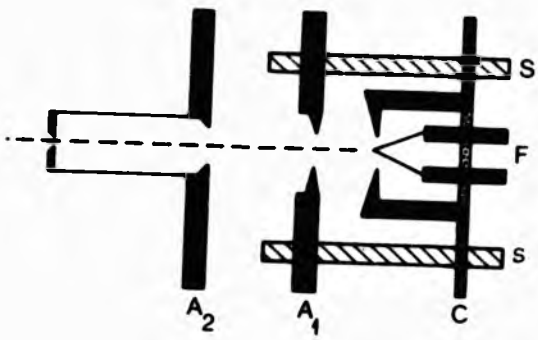

Figure 3.2(a): The electron gun. F is a hairpin shaped filament, C is the cathode, A_1 the focussing electrode, A_2 the collimating electrode, and parts marked S are the ceramic rods.

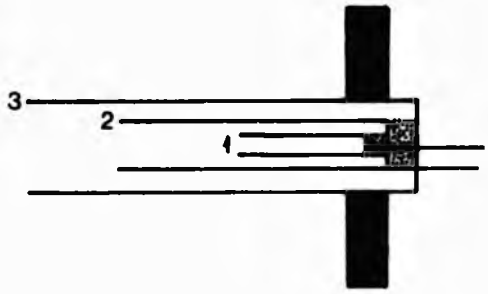

Figure 3.2(b): The Faraday cup. 1, 2 and 3 are the three concentrically placed aluminium cylinders separated by boron nitride spacers.

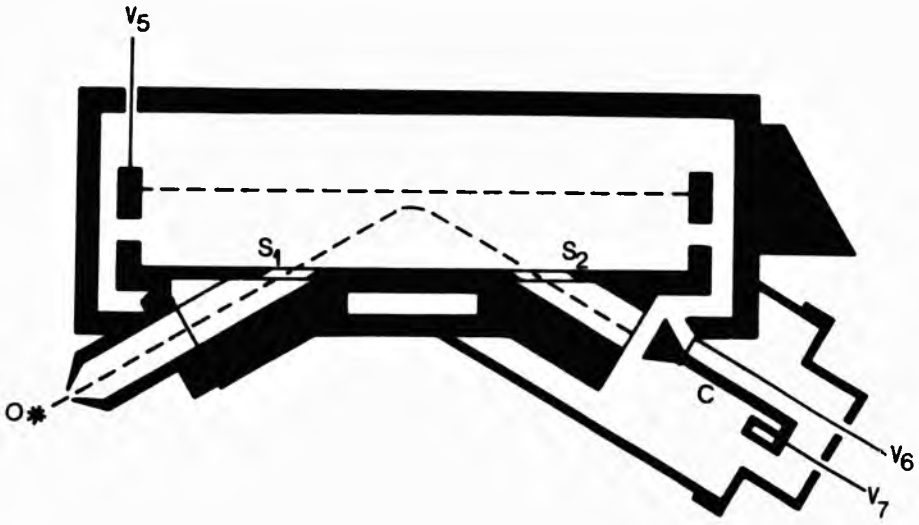

Figure 3.4(a): The electron analyser. O is the interaction region, S_1 and S_2 are the defining slits and C is the channeltron used for the detection of electrons (see text for detailed discussion).

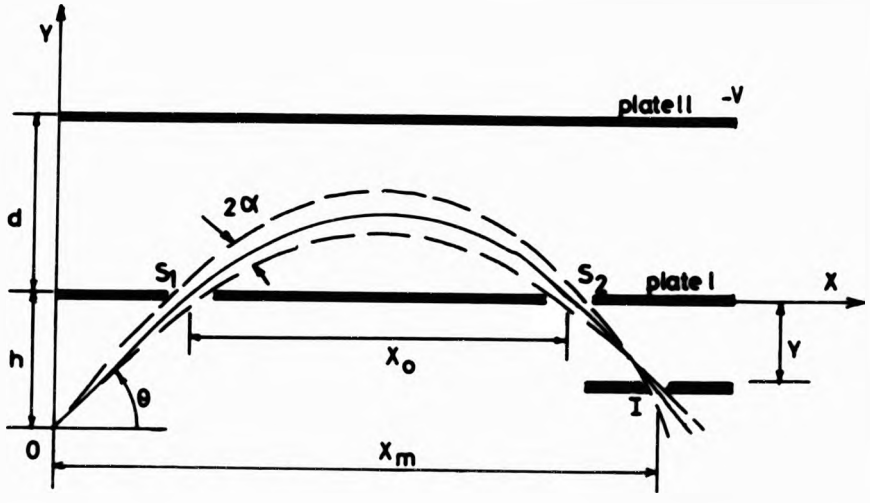

Figure 3.4(b): Electron path in a parallel plate electrostatic analyser (see text for explanation).

consisting of a needle valve and a pressure regulator fixed to the rare gas cylinder. Any gas pressure can be obtained inside the vacuum chamber by regulating the gas supply system.

Gas pressure in the collision region is adjusted to be low enough to ensure single collision conditions (Nagy et al. 1980). For helium, neon and argon, pressure was 5.0×10^{-6} torr and for krypton and xenon 4.0×10^{-6} torr. Research grade gases supplied by BOL were used.

3.4 Electron Analyser

Figure 3.4(a) shows schematically the 30° parallel plate analyser which has been used for the analysis of electrons ejected as a result of interaction of electrons with gas atoms. It has been built from non-magnetic stainless steel. A wire mesh, made from 0.1 mm thick tungsten wires, spot-welded 1 mm apart on a supporting frame, acts as the upper plate for the deflection of electrons inside the analyser. The potential difference between the mesh and the lower plate defines the energy of the selected electrons. The analyser elements and the channeltron are covered by light-tight shielding to avoid stray electrons entering the analyser. Boron nitride and PTFE spacers are used for the insulation of the upper plate and the channeltron.

The trajectory of electrons of energy E = eU, and making an angle θ with the x-axis, is shown in Figure 3.4(b). If d is the separation of the plates, V the potential difference between the plates I and II, h and y are distances of the source and the image from plate I, then the equation describing the electron path in the field-free region inside the analyser is (Green and Proca, 1970)

$$x(\theta,V,h) = (h + y)\cot\theta + \left(\frac{2dU}{V}\right)\sin 2\theta \qquad 3.4\text{-}1$$

where x is measured from the end of the analyser as shown in Figure 3.4(b). For the analyser to have first and second order focussing

properties then it is required that

$$\frac{\partial x}{\partial \theta} = 0 \text{ and } \frac{\partial^2 x}{\partial \theta^2} = 0$$

$$\theta = 30° \text{ and } \frac{dU}{hV} = 2.$$

The ratio U/V is called the analyser factor, f. Thus

$$f = U/V = {}^{2h}/_{d} \qquad 3.4\text{-}2$$

According to Schmitz and Mehlhorn (1972) any parallel plate analyser will have second order focussing property if it satisfies the condition $0 < y < h$.

The analyser resolution is given by (Green and Proca, 1970)

$$\frac{\Delta U}{U} \simeq 1.6(\alpha)^2 \qquad 3.4\text{-}3$$

for a 30° parallel plate analyser. Green and Proca, 1970 have compared this analyser with other analysers and have shown that while this analyser has double focussing property, other type of analysers are mostly monochromators.

The analyser transmission, T, is given by

$$T = \frac{\Delta\phi}{4\pi} (\sin\theta_{max} - \sin\theta_{min}) = (\frac{\delta\phi}{2\pi}) \cos\bar{\theta} \sin\alpha \qquad 3.4\text{-}4$$

where $\Delta\phi$ is the angular width in the transverse plane and $\theta_{max} = \theta + \alpha$, $\theta_{min} = \theta - \alpha$.

For $\Delta\phi = 2\pi$, the transmission is given by

$$T = \frac{\sqrt{3}}{2} \sin\alpha. \qquad 3.4\text{-}5$$

Green and Proca (1970) and Proca and Green (1970) have given a detailed discussion about other characteristics of this analyser.

As shown in Fig. 3.4(a) the negative voltage V_5 given to the grid of the analyser determines the energy of the electrons which are focussed at the cone of the channeltron. The lower plate of the analyser is kept at ground potential. As the detection efficiency of a channeltron varies with the energy of the detected electrons, for maximum detection efficiency it was necessary to ensure that the electrons were incident at the surface of the cone of the channeltron with a constant energy of 200 eV. To achieve this condition V_6 was made positive or negative and was adjusted to keep the incident electron energy around 200 eV. In addition V_7 was adjusted to keep the potential difference between V_6 and V_7 the same throughout the experiment thus keeping the gain of the channeltron nearly constant.

3.5 Ion analyser

The ions formed as a result of ionization are analysed with respect to their charge (mass being the same) by a time-of-flight (TOF) method. Ions from the interaction region are pulled into the ion analyser by a weak electric field. These ions are accelerated further until they acquire the desired kinetic energy whereupon they enter and are allowed to drift in a field free region (35 mm). Finally they are accelerated to several keV energy before they impinge on the channeltron surface for detection.

Fig. 3.5(a) shows the analyser schematically. Concentrically, placed cylindrical tubes, made out of non-magnetic stainless steel have at their ends grids formed by welding together 0.2 mm diameter tungsten wire. These tubes are fixed to an aluminium housing containing the channeltron (Mullard 913B). PTFE spacers are used to insulate the drift tubes from the channeltron housing and from each other.

If the distance D travelled by ions inside the drift tubes is large compared to the distance between the interaction region and the

tube opening then for an ion of mass M, charge ne and velocity v_n, the time of flight t_n is given by

$$t_n = \frac{D}{v_n} = \left(\frac{MD^2}{2eV}\right)^{\frac{1}{2}} \times \frac{1}{n^{\frac{1}{2}}} \qquad 3.5\text{-}1$$

where V is the voltage through which the ion has been accelerated to attain velocity v_n.

For an experiment with any gas the quantity $\frac{MD^2}{2eV}$ remains constant and the time of flight t_n is thus indirectly proportional to $n^{\frac{1}{2}}$. Thus, mass being the same, ions having different charge states should separate out in the form of a spectrum, such as the one shown in Fig. 3.5(b).

Any initial kinetic energy that an ion possesses, whether thermal energy of a parent atom or kinetic energy released in the formation of an ion has a strong effect on the flight time. An ion with initial velocity in the forward direction will arrive too soon while one which starts off in the opposite direction must be retarded to stop, then returned to its starting position with a reversed velocity. The difference in arrival time between these two extreme ions is just twice the retardation time. The effect of initial kinetic energy in time-of-flight mass spectrometers has been studied by Franklin, Hurl and Whan (1967) who have shown that for small initial kinetic energies compared with the energy acquired in the field, the greatest and least flight times are symmetrical about the flight time of an ion from the centre of the interaction region and with zero initial velocity. There is then one-to-one correspondence between arrival times and initial velocities in the flight direction and, for a Maxwellian initial energy distribution, the shape of the peak in a time-of-flight spectrum is a Gaussian with a width $W_{\frac{1}{2}}$ at half maximum given by

$$W_{\frac{1}{2}} = 1.664(2kTM)^{\frac{1}{2}} / eE \qquad 3.5\text{-}4$$

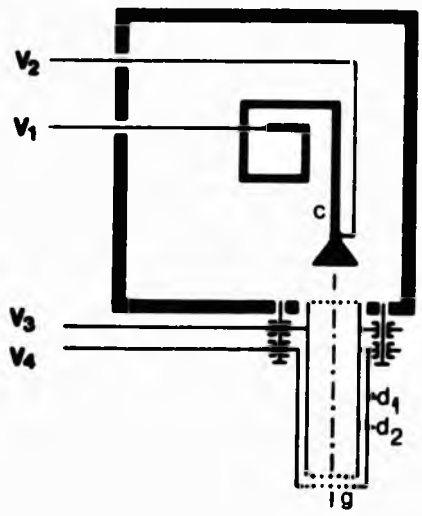

Figure 3.5(a): The ion analyser. d_1 and d_2 are the two concentric cylindrical drift tubes, insulated from each other. The tungsten wire grids are marked g and c is a channeltron.

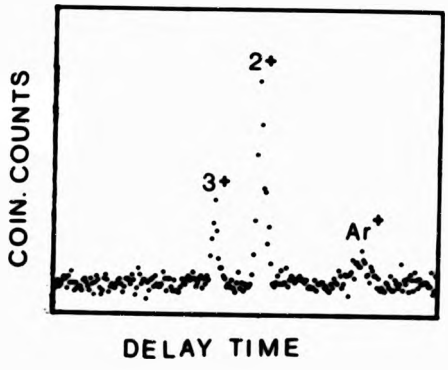

Figure 3.5(b): Typical TOF spectrum of argon ions. Peaks for Ar^+, Ar^{2+} and Ar^{3+} can be seen.

where k is the Boltzman constant, T is the temperature (K°), M is mass of the ion in atomic mass units and E is the electric field in volts cm^{-1}.

This result is applicable to time-of-flight coincidence spectroscopy. Equation 3.5-2 shows that a thermal ion of mass 40 a.u. at 300°K in a field of 15 volt cm^{-1} should have a delay half-width $W_{\frac{1}{2}}$ of about 0.2 μs. This is a fundamental limitation on coincidence resolving times. The spread of ion flight time can be reduced by increasing the extraction field in the interaction region, but doing so necessarily worsens the electron energy resolution. The ionization region itself must have a definite width, δS, in the field direction which gives the electrons a minimum energy spread, $E.\delta S$. The conditions of any experiment must be a compromise, chosen between time resolution for coincidence and energy resolution for electrons. The situation can be improved by making the ionization region as small as possible and by providing the target gas in the form of an atomic beam.

The electronic circuit for the analyser is shown in Fig. 3.5(c). V_1 is a low voltage (between 15-25 volts) which draws ions out of the interaction region while V_2 (between 25-100 volts) gives the ions a higher energy. Having attained the desired speed in the field-free region inside the drift tubes, at the end of the drift region, voltage V_3 at the cone of the channeltron gives the ions enough energy to be efficiently detected in the channeltron. Ravon (1982) has shown how the detection efficiency of a channeltron for various ions having different charge states varies with the ion energy. For almost all ions having energy of about 4 keV, the detection efficiency exceeds 80%. If, therefore, V_3 is kept at about 4 kV then V_4 can be varied to adjust the potential difference across the channeltron to maintain the conditions for optimum gain.

3.6 High voltage power supplies, MCA and other electronic equipment

For the purpose of accelerating electrons, a high voltage with a negative polarity was supplied to the cathode of the electron gun by a regulated (0.2%) Universal Voltronics (Model BRE-20.25-R2) power supply. The filament heating power supply and the anode power supply were isolated using an isolation transformer. An E.G. & G. Ortec multichannel analyser (MCA) was used in the pulse-height analysis (PHA) mode to record the time spectra for these coincidence studies. Standard NIM units (Ortec & NE) were used for signal amplification and discrimination etc.

3.7 Hyperpure germanium (HPGe) X-ray detector

The x-ray detector used for spectroscopy was an E.G. & G. Ortec 1000 series low energy photon spectrometer (LEPS). It is essentially a diode made from a hyperpure germanium (HPGe) crystal (impurities less than 10^{10} atoms/cm^3) and is operated at liquid nitrogen temperature. The detector has dimensions of 6 mm active diameter by 5 mm active depth. The beryllium entrance window is 0.0254 mm thick. The front electrode of the detector is ion implanted to obtain a thin, robust and reliable contact.

When an x-ray photon is absorbed in the detector, it produces electron hole pairs (on average it requires 2.95 eV per pair), which are swept out of the detector volume by the electric field due to the bias voltage (1200 volts). The resulting current pulse is integrated by a charge sensitive preamplifier. The first transistor of the preamplifier is cooled to minimise electronic noise. The amplitude of the integrated current pulse is proportional to the energy lost by the incident x-rays inside the detector. Figure 3.6(a) shows a graph of detection efficiency versus photon energy for a HPGe detector of various sizes having windows of different thicknesses.

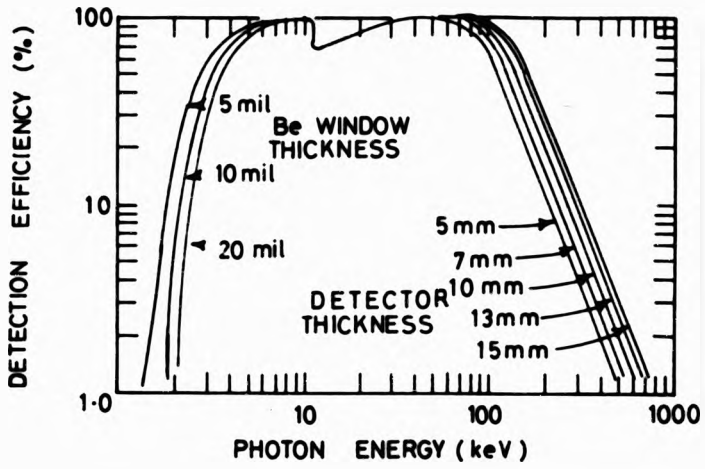

Figure 3.6(a): Detection efficiency curves for HPGe detectors of different thickness and having different thickness beryllium windows. (1 mil = 0.025 mm).

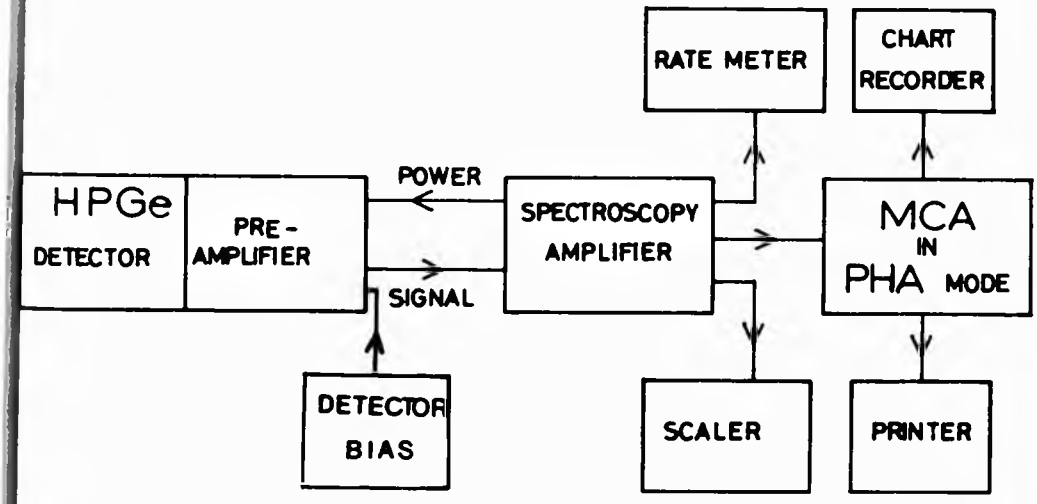

Figure 3.6(b): Electronic circuit for HPGe detector.

3.8 Crystal x-ray spectrometer

3.8.1 Principle

Bragg's law $n\lambda = 2d \sin\theta$ relates the wavelength λ of the incident x-ray to the angle θ at which a coherent diffraction pattern is formed. Here d is the crystal lattice spacing and n is an integer which gives the order of reflection. The simplest device uses a planar crystal, Soller slits for x-ray collimation and a proportional counter for x-ray detection.

The angular dipersion D_θ for a Bragg spectrometer is given by

$$D_\theta = d\theta/d\lambda = (\tan\theta)/\lambda = \frac{n}{2d} \sec\theta \ . \qquad 3.8.1\text{-}1$$

From equation 3.8.1-1 it can be seen that high dispersion is obtained for larger θ, or at backward angles. Also, for a given crystal, better resolution can be obtained, in general, by measuring the x-rays in a higher order.

The energy resolution of a crystal spectrometer is obtained from the derivation for $d\lambda/d\theta$ and can be expressed as

$$\Delta E/E = \cot\theta \Delta\theta \qquad 3.8.1\text{-}2$$

The angular resolution $\Delta\theta$ is determined by the instrumental resolution and by the angular spread (usually less than 0.1°) corresponding to the rocking curve (Werner,1983) of the crystal. The rocking curve is a measure of the angular range over which diffracted monochromatic x-rays are spread due to crystal imperfections. It follows from equation 3.8.1-2 that the energy resolution worsens with increasing x-ray energy. Thus, while crystal spectrometers provide an excellent resolving power ($\sim 10^3$) at low photon energy, they become inferior to energy dispersive solid-state devices for energies above 20 keV.

3.8.2 The Instrument

Figure 3.8.2(a) shows the spectrometer schematically. M is a three phase stepping motor (Sigma Instrum.) which rotates a shaft S by the help of a flexible belt R. The shaft S rotates the crystal K, mounted on a plastic holder, around axis of rotation A, in steps of ∿0.01°. A Soller collimator, held in place by a holder H, collimates the beam of x-rays to an accuracy of 0.075°. The reflected x-rays enter the sensitive volume of a proportional counter through its thin window F. A 20-turn potentiometer is fixed to the shaft S by a flexible coupling for locating the crystal position. The spectrometer can be fixed to the vacuum chamber by a 4" flange and can be made vacuum tight.

2.8.3 Collimation of x-rays

The collimation of x-rays is done by passing the x-rays through a Soller-slit-system. This is an arrangement of plane parallel metal plates uniformly separated to allow well-defined parallel beams of x-rays. The divergence of the beam of x-rays is given by

$$\tan \epsilon = \frac{S}{\ell}$$

where d is the thickness of the Soller plates, S the distance between them and ℓ is their length as shown in Fig. 3.8.3(a).

A good collimation (2ϵ=0.075°) has been attained with a Soller collimator (Siemens AG) using plates having ℓ = 150 mm, S = 0.10 mm and d = 0.10 mm. An analysis of x-ray transmission by various Soller collimators has been carried out by Harbach (1980).

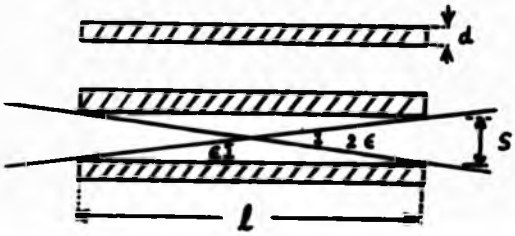

Figure 3.8.3(a)

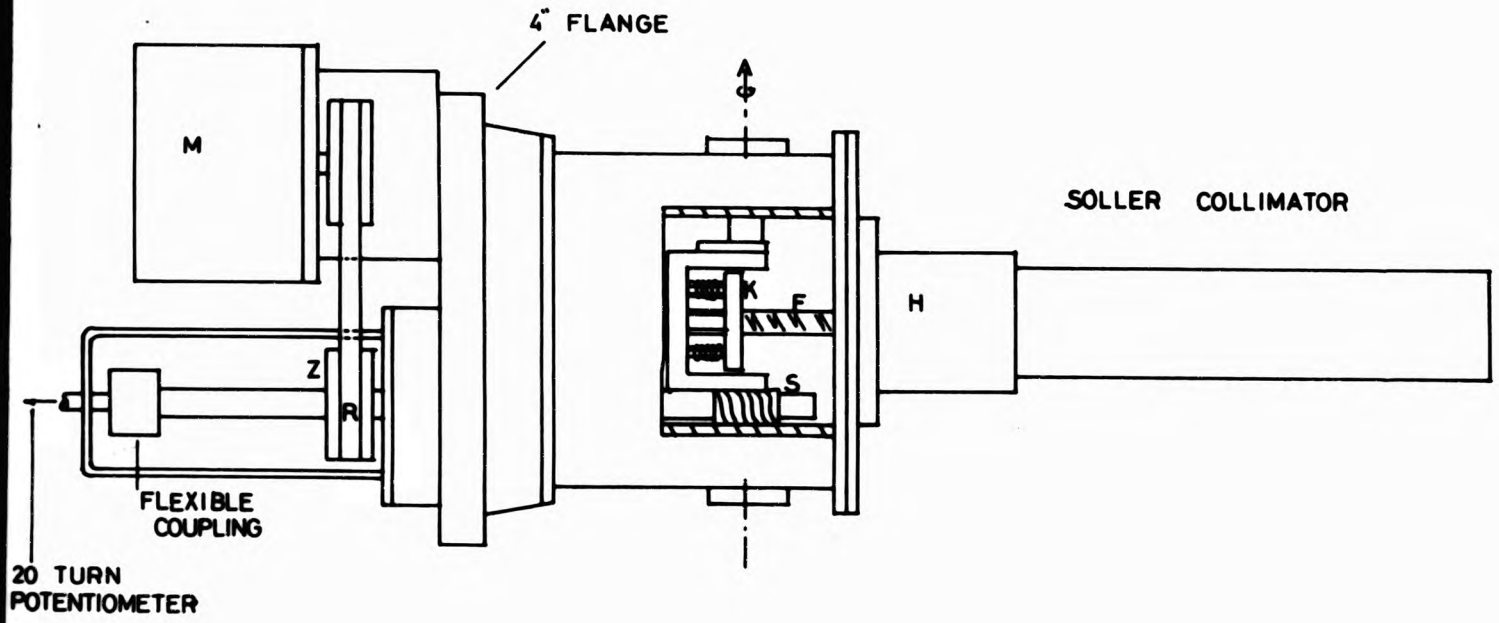

Figure 3.8.2(a): The crystal x-ray spectrometer. K is the crystal, F the proportional counter, S the shaft responsible for rotating the crystal, H the holder for the Soller collimator, M the stepping motor and R the flexible belt.

3.8.4 Crystal

Incident x-rays are reflected specularly by a crystal as shown in Fig. 3.8.4(a). The reflectance for a ray incident at a glancing angle θ is denoted by C W $(\theta-\theta_B(\lambda))$, (Morita, 1983) where C is a constant, $W(\theta-\theta_B(\lambda))$ is a function whose curve is called the rocking curve, and $\theta_B(\lambda)$ is the Bragg angle, which satisfies Bragg's law $2d \sin\theta_B(\lambda) = n \lambda$. Here, λ is the wavelength of the incident ray, d the spacing of the crystal lattice, n the order of diffraction.

If a collimated beam of x-rays is incident on a crystal then intensity distribution of an x-ray spectrum can be measured by a detector placed at the corresponding angle on the opposite side of the normal. The system effectively selects all rays which are incident at the appropriate angle of Bragg reflection. If the angle of incidence is then varied (by rotating the crystal by a controllable angle and the detector by twice this amount) the detector will receive radiation of a different wavelength at a different angle and a spectrum will thus be obtained.

The resolution of such a spectrometer depends, in part, on the geometrical definition provided by the slit. A further limit is imposed by the intrinsic resolution of the crystal. If the incident radiations were truly monoenergetic, the peak obtained in the spectrum would be that for the crystal alone. In practice, characteristic x-ray lines are found to have a finite width, which is related to the lifetime of the state by the uncertainty principle. The natural widths of the x-ray lines can be studied by spectrometers having higher resolution.

The natural resolution of crystals depends upon the degree of alignment of the surface atomic planes. For mosaic crystals to be suitable for spectrometry, they should have a narrow rocking curve

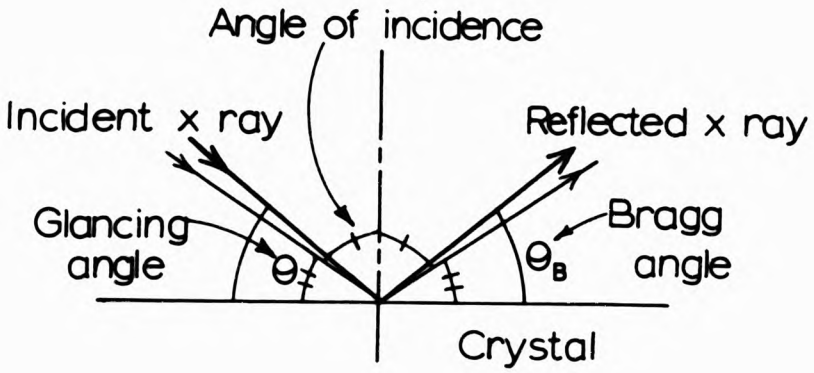

Figure 3.8.4(a): Reflection of x-rays by a plane crystal.

combined with a high integrated reflection coefficient (the reflection coefficient integrated over the angular width comprising the rocking curve (Werner, 1983; Birks, 1978)).

A list of analysing crystals is given in table 3.8.4(1) showing their main characteristics together with the lowest atomic number detectable in each case

Table 3.8.4(1) Analysing crystals (Jenkins and de Vries, 1970)

Crystal	Reflection plane	2d spacing (Å)	Lowest atomic number detectable		Reflection efficiency
			K series	L Series	
Topaz	(303)	2.712	V(23)	Ce(58)	Average
Lithium fluoride	(220)	2.848	V(23)	Ce(58)	High
Lithium fluoride	(200)	4.028	K(19)	In(49)	Intense
Sodium chloride	(200)	5.639	S(16)	Ru(44)	High
Quartz	$(10\bar{1}1)$	6.686	P(15)	Zr(40)	High
Quartz	$(10\bar{1}0)$	8.50	Si(14)	Rb(37)	Average
Penta erythritol	(002)	8.742	Al(13)	Rb(37)	High
Ethylenediamine tartrate	(020)	8.808	Al(13)	Br(35)	Average
Ammonium dihydrogen phosphate	(110)	10.65	Mg(12)	As(23)	Low
Gypsum	(020)	15.19	Na(11)	Cu(29)	Average
Mica	(002)	19.8	F(9)	Fe(26)	Low
Potassium hydrogen phthalate	$(10\bar{1}1)$	26.4	O(8)	V(23)	Average
Lead stearate		100	B(5)	Ca(20)	Average

The double spectrometer is in wide use for examination of line profiles at ordinary wavelengths because the dispersion available is twice that of a single crystal spectrometer and the resolution is also improved.

3.8.5 Proportional Counter

The proportional counter is a special form of ionization chamber in which a single ionizing event produces an output pulse which has been increased 10^4 - 10^7 times (Fink, 1975), due to electron multiplication in the high electric-field region surrounding the central anode wire. If the field gives enough energy to a free electron between collisions with the gas to cause additional ionization then multiplication occurs.

In a coaxial cylindrical counter having an anode wire of radius a and cylindrical cathode of radius b, the electric field E at any distance r from the centre is given by

$$E = V/[r \log_e (\frac{b}{a})] \qquad 3.8.5\text{-}1$$

where V is the total applied voltage. This shows that the region where an electron gains sufficient energy between collisions to cause further ionization lies only within a few diameters of the centre wire, so that the output pulse height is essentially independent of the location of the initial ionizing event in the counter volume.

The gas amplification M can be defined as the number of electrons collected at the centre wire per primary electron released in the original ionizing event. The specific ionization $\alpha(r)$ is the mean number of secondary electrons produced by an electron per centimeter of its path. The specific ionization is taken as the

reciprocal of the mean free path between ionizing collisions which is a function of the radial distance r from the centre. Gas amplification and specific ionization are related by

$$\log M = \int_{a}^{r_c} \alpha(r)\,dr \qquad 3.8.5\text{-}2$$

where r_c is the critical radius where multiplication first begins.

It can be shown (Gold and Bennett, 1966) that the energy resolution of a proportional counter is determined largely by the gas amplification, which in turn depends critically on the counter wire radius. Also, the quality of the centre wire, i.e. its smoothness and uniformity, is important for good resolution.

The energy resolution ΔE of a proportional counter is to a large extent determined by the statistics of the ionization processes taking place in the counter gas. For an x-ray peak with energy E, the energy resolution defined as full width at half maximum (FWHM) due to collection statistics is given by Mokler et al. (1978). A typical value of the energy resolution of a proportional counter is 830 eV at an x-ray energy of 6 keV (Mokler et al. 1978).

It has been observed (Culhane et al. 1966) that the rise-time of the pulses originating from x-rays is rather faster than those due to high energy electrons or mesons. This appears to be due to the short range of photo-electrons with the consequence that all the ion-pairs produced by the absorption of an x-ray photon originate in a closely defined region of the counter, causing the electrons to have transit times which are closely similar. The difference in rise-time has been used (Campbell, 1968; Lewyn, 1970 and Isozumi & Isozumi, 1971) in the x-ray region 6-15 keV, for example, to reject more than 90% of the background while more than 95% of the x-ray

signals are retained by the system. Rise-time discrimination of x-rays from particle events is discussed in an article by Culhane and Fabian (1972).

The proportional counter used in this experiment has an active length of ∿ 7cm, cathode diameter 2.1cm and tungsten wire of diameter 0.1mm. The operating potential is 1500 volts.

3.8.6 Controlling the spectrometer with a microcomputer

Figure 3.8.6 shows a circuit for controlling the stepping motor and an MCA by a BBC microcomputer. A stepping motor rotates the crystal by the help of a gear system in steps of about 0.01 degree. To scan a particular angular region, the stepping motor is first moved to the start of the region of interest. Then an appropriate number of channels are selected. The MCA is put in MCS mode and in external control position. The computer is then made to run the programme given in the Appendix. Automatically the MCA is put in collect mode and at each step counts from the x-ray detector are stored in a different channel. At the end of each scan the MCA is put out of the collect mode and the stepping motor moves the crystal back to its original position. It can repeatedly scan this region as many times as asked and thus can go on building up the x-ray spectrum.

INTERFACING STEPPING MOTOR AND AN M.C.A. TO A BBC MICRO-COMPUTER

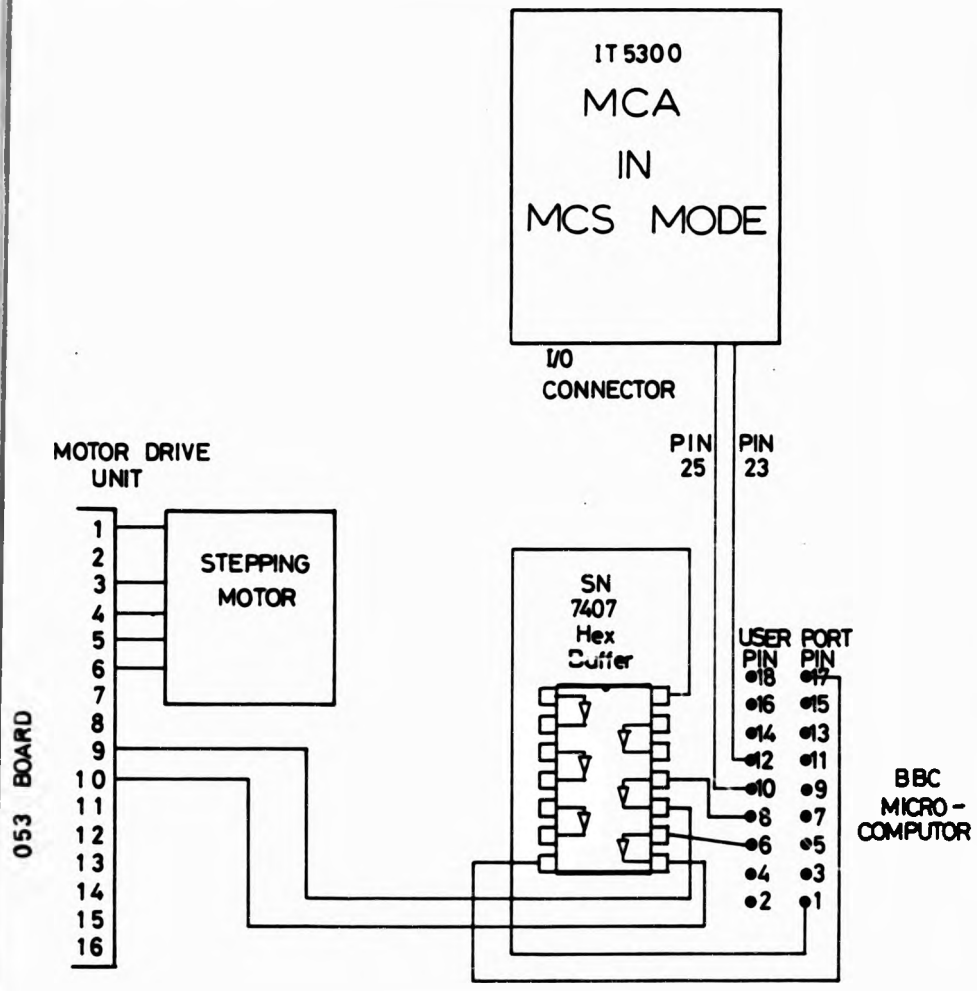

Figure 3.8.6(a): Circuit for controlling the stepping motor and and MCA by a BBC-microcomputer.

CHAPTER 4

EXPERIMENTAL TECHNIQUE

4.1 Electron-ion coincidence technique

Figure 4.1(a) shows schematically the experimental set up for the electron-ion coincidence experiment to study the electron-atom collision process and to measure DDCS and DDCS(n+). A focussed beam of energetic electrons (§ 3.2) is allowed to interact with a beam of atoms emitted by a capillary array (§ 3.3). The Faraday cup (§ 3.2) collects the electron beam efficiently. The diameters of the beams of atoms and electrons are each about 2mm. The interacting electrons are monoenergetic while the atoms have a thermal energy distribution. Electrons ejected at 90° to the two beam directions and in a solid angle $\Delta\Omega$ are accepted by a 30° parallel plate electrostatic analyser (§ 3.4). Energy analysed electrons are detected by a channeltron. To select ejected electrons having energy E(eV) a deflecting voltage of 0.6 E(Volt) has to be applied to the upper plate of the analyser. Electric potentials at the channeltron are varied so that the electrons incident at the channeltron always have an energy of 200 eV for maximum detection efficiency (Mullard databook). Figure 4.1(b) shows an output pulse from the electron analyser.

Figure 4.1(b). Output pulse from the electron analyser. Δt = 0.01 μsec and ΔV = 40 millivolts.

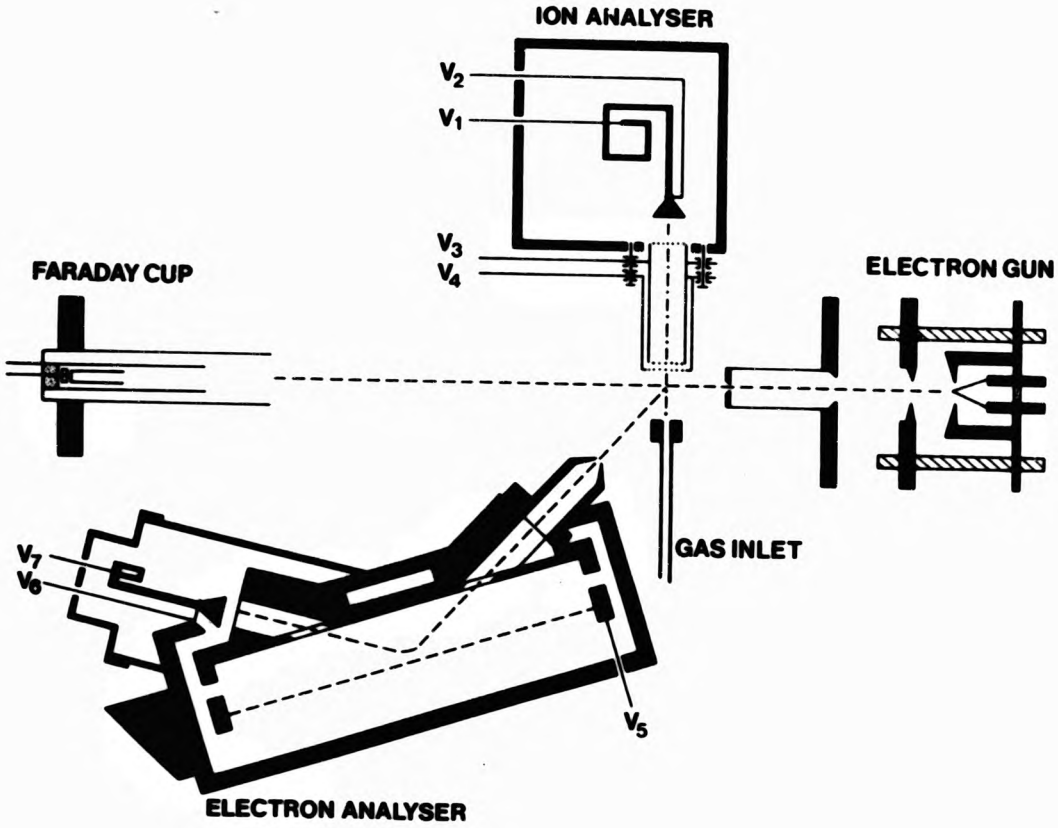

Figure 4.1(a): Experimental set up for electron-ion coincidence experiments.

Ions produced by the collision process are extracted by a small electric field between 15V and 25V per centimetre and are directed into a time-of-flight (TOF) type analyser (§ 3.5). Inside the ion-analyser, ions are further accelerated before they drift in a field-free region, 35 mm long, inside the drift tube. At the end of the drift region the ions are accelerated by a suitable high voltage at the cone of the channeltron for high efficiency of detection (Ravon, 1982). Potential, V_7, at the closed end of the channeltron can be varied to keep the amplification of the channeltron constant throughout an experiment. Figure 4.1(c) shows an output pulse from the ion-analyser.

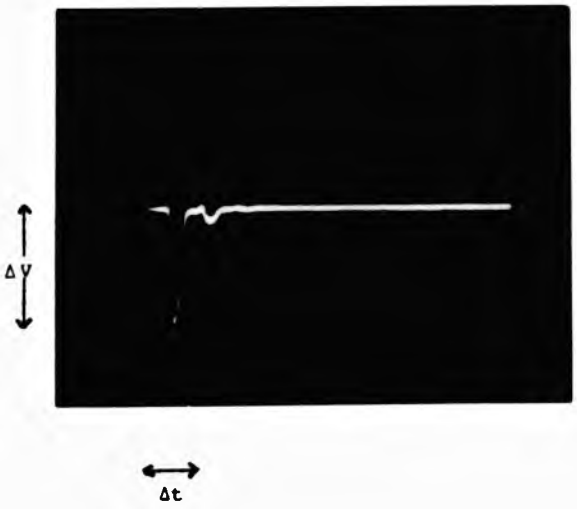

Figure 4.1(c): Output pulse from the ion-analyser. Δt = 0.05 microsecond and ΔV = 30 millivolts.

Figure 4.1(d) shows the electronic set up for measuring coincidences between ejected electrons and the ions produced in the collision process. Pulses from the electron-analyser are amplified and fed to a timing discriminator which supplies a prompt pulse suitable for the "start" of a time-to-amplitude converter (TAC). Also, amplified pulses from the ion-analyser are fed to the input of a snap-off timing discriminator. The negative output of the timing discriminator is used to

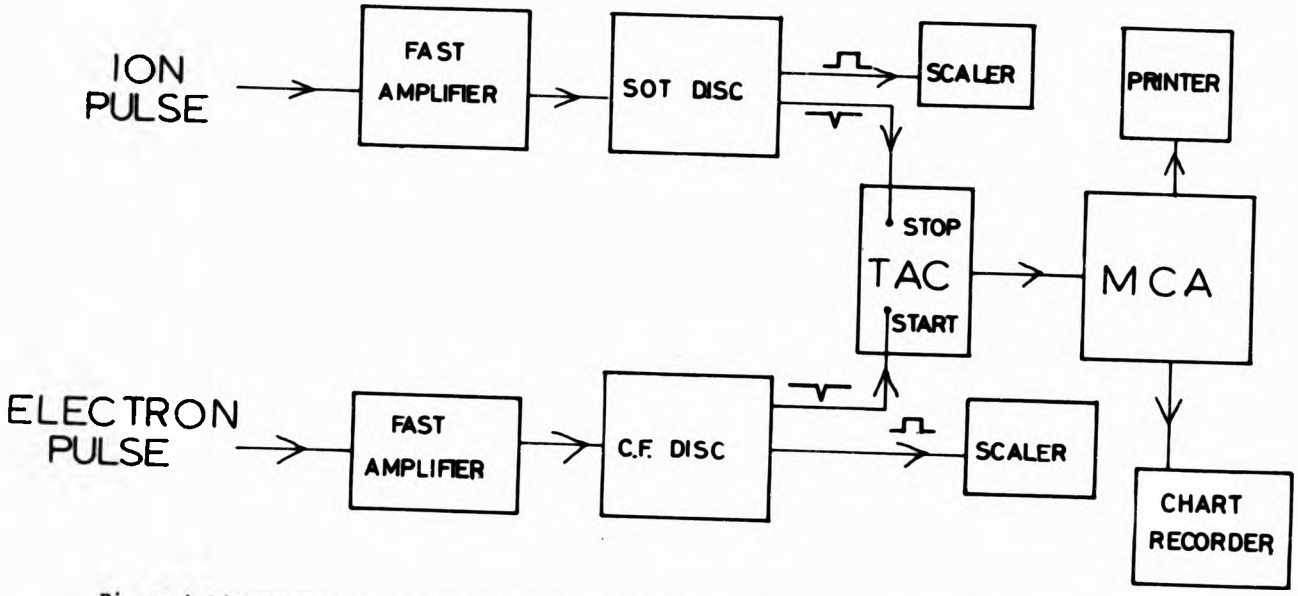

Figure 4.1(d) Electronic circuit for electron-ion coincidence spectroscopy.

stop the TAC. The time delay between the pulses from an ion and the ejected electron gives information about the charge state of the detected ions. Figure 4.1(e) shows such a time spectrum for argon. Peaks for charge state 1+ to 4+ can be seen. Delay time (t_n) for the arrival of an ion charge n+ is inversely proportional (equation 3.5-1) to the square root of n, in any such spectrum

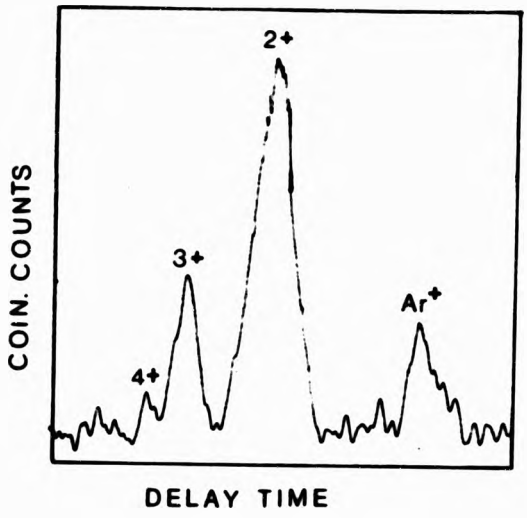

Figure 4.1(e):

TOF spectrum for argon ions.

4.2 X-ray-ion coincidence technique

Figure 4.2(a) shows schematically the experimental set up used for the x-ray-ion coincidence experiment. A focussed beam of accelerated electrons from an electron gun (§3.2) are crossed with a beam of thermal atoms emitted by a capillary array (§3.3). Innershell ionization of atoms results in the emission of characteristic x-rays (§2.2) which are detected by a hyper-pure germanium (HPGe) detector (§3.7).

Ions produced as a result of the collision process are extracted by a small field of about 25 volt cm^{-1} and are directed into a time-of-flight (TOF type analyser described in detail in section 3.1).

Figure 4.2(b) shows the electronic set up for measuring coincidences between the ions and the emitted x-rays. X-ray pulses from HPGe are fed to the timing filter amplifier (TFA) (Ortec 474). A fast negative pulse from the TFA is used as a start pulse for the time-to-amplitude

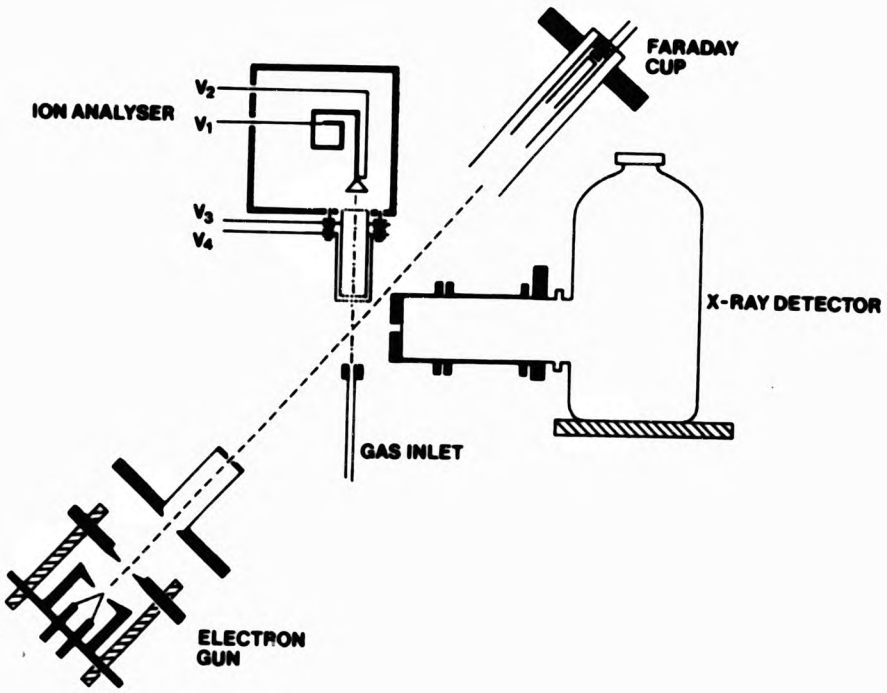

Figure 4.2(a): Experimental set up for x-ray-ion coincidence spectroscopy.

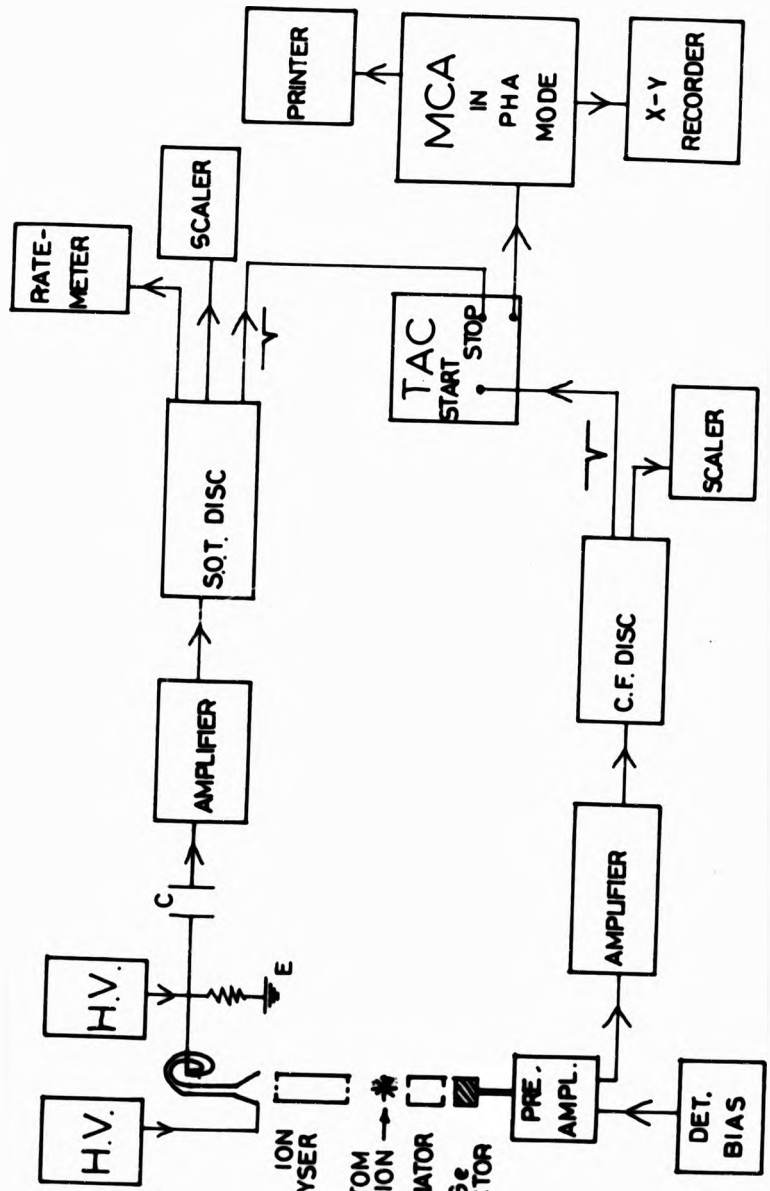

Figure 4.2(b): Electronic circuit for x-ray-ion coincidence experiments.

converter (TAC) (Ortec 467). A stop pulse for the TAC comes from the ion, which is detected by the ion-analyser. The output pulse from the TAC is fed to an MCA in pulse height (PHA) mode. A delay time spectrum for x-ray-ion coincidences is built up in the MCA. The time delay between the detected x-ray and the ion gives information about the charge state of the product ion.

4.3 Crystal x-ray spectrometer

Figure 4.3(a) shows the crystal x-ray spectrometer set up for the spectroscopy of ^{54}Mn, $K\alpha_1$ and $K\alpha_2$ lines from the decay of ^{55}Fe radioactive source. The x-ray source is placed in front of the Soller collimator (§3.8.3). The collimated beam of x-rays is incident on a Na Cℓ(100) or LiF(200) crystal mounted on a plastic base. The crystal can be rotated by 0.01° steps with the help of a stepping motor and a gear system. The x-rays reflected according to the Bragg Law are detected by a constant gas flow type proportional counter (§3.7.5). Argon methane mixture (90% Ar, 10% methane) flows through the counter constantly at a rate of ∿ 15 ml/min.

Figure 4.3(b) shows the electronic circuit for controlling the stepping motor and MCA with the help of a BBC microcomputer. When the program given in Appendix is run in the computer, the MCA is switched to collect mode and then with each step of the stepping motor the next channel of the MCA (in MCS mode) is made to collect the counts from the detector. At the end of the scanning region, the MCA is switched out of the collect mode and the stepping motor brings the crystal to its original angular position, ready for the next scan. The time for each channel and the number of scans can be controlled to build up a spectrum in the MCA.

BLOCK CIRCUIT FOR CRYSTAL X RAY SPECTROMETER

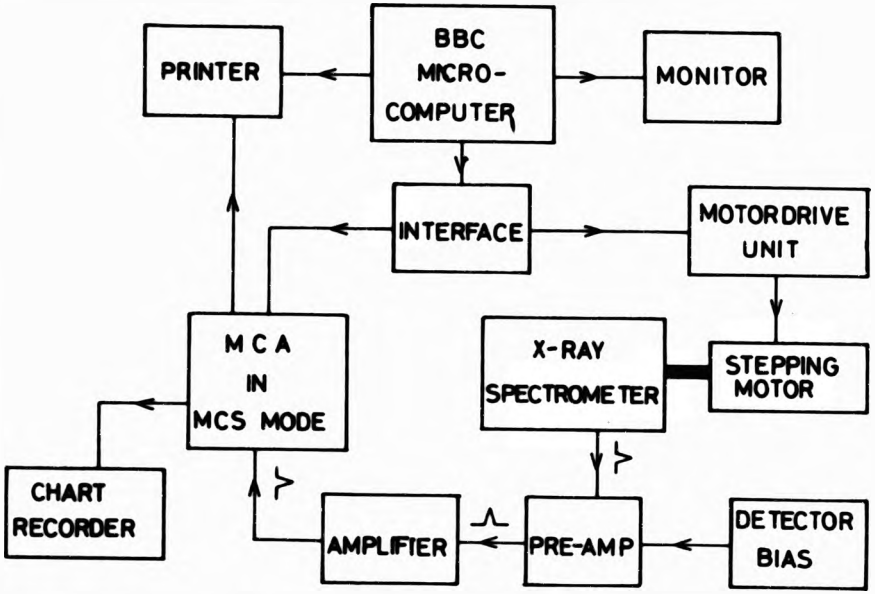

Figure 4.3(a): Electronic circuit for the crystal x-ray spectrometer.

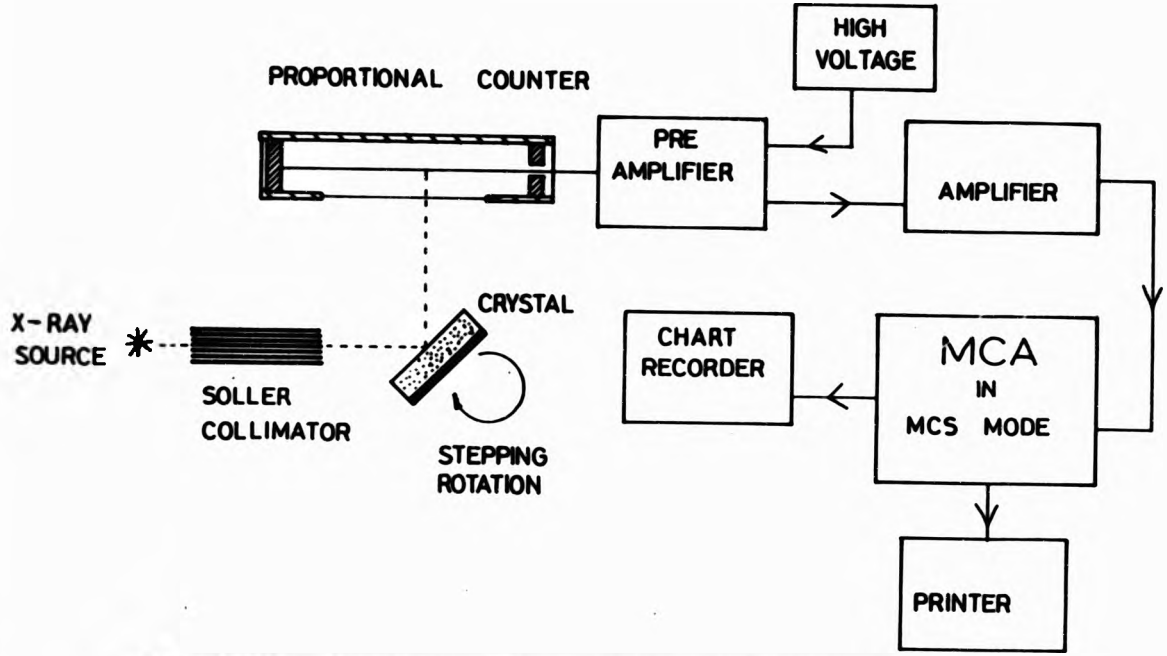

Figure 4.3(b): Electronic circuit for crystal x-ray spectrometer.

CHAPTER 5

RESULTS AND DISCUSSION

5.1 Electron-ion coincidence experiments

The electron-atom collision process,

$$e + X \rightarrow X^{n+} + ne + e_{\delta}$$

where X stands for a rare gas atom, has been investigated for multiple ionization events. Detection of secondary electron (hereafter called a δ-electron, e_{δ}) in coincidence with the product ion, X^{n+}, allows the identification of n-fold ionization process. As it is, however, not possible, in these experiments, to differentiate between the secondary or ejected electron (e_{δ}) and the primary electron which has lost a great deal of its energy, the secondary electrons must be taken to include all electrons of the selected energy.

The experimental arrangement used for these experiments is described in section 4.1, where a typical TOF spectrum is also shown. From such a spectrum after subtraction of random coincidences the number of true coincidence events, $N_c^{(n)}$, is related to a double-differential cross section for n-fold ionization, $d^2\sigma^{(n)}/(dEd\Omega)$, by

$$\frac{d^2\sigma^{(n)}}{dEd\Omega} = \frac{N_c^{(n)}}{N_i} \frac{\sigma_i}{\Delta E \Delta \Omega \varepsilon_{\delta}} \qquad 5.1\text{-}1$$

where σ_i is the total cross-section for ion production, N_i the number of detected ions and ε_{δ} the efficiency of the electron detection system. ΔE and $\Delta\Omega$ are the energy band width and the solid angle of the electron analyser, respectively. For σ_i, the experimental values were taken from Schram (1966). No attempt was made to evaluate the factor $\Delta E \Delta \Omega \varepsilon_{\delta}$ but it was endeavoured to keep it constant during the course of these investigations by adjusting the voltages at the ends of the channeltron in the electron analyser so that electrons are always incident on the channeltron with an energy of 200 eV, for maximum detection efficiency.

The double-differential cross section (DDCS) was also found by summing the partial-double differential cross sections (DDCS(n+))

over all values of n, i.e.

$$DDCS = \sum_n DDCS(n+) \quad . \qquad 5.1\text{-}2$$

Also the mean charge $\bar{n}(E)$, for ions in coincidence with the secondary electrons of energy E, is given by

$$\bar{n}(E) = \left(\sum_n N_c^{(n)} n\right) \Big/ \sum_n N_c^{(n)} \qquad 5.1\text{-}3$$

5.1.1 Helium

Figure 5.1.1(a) shows a TOF spectrum for helium. A very strong peak for He^+ and a very weak peak for He^{++} can be seen.

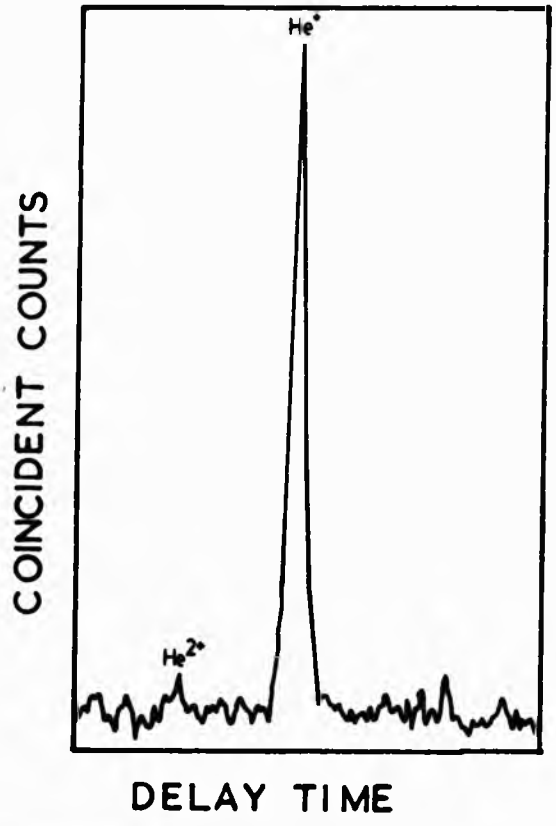

Figure 5.1.1(a)

TOF spectrum for helium ions (He^+ and He^{2+}) detected in coincidence with ejected electrons of energy 100 eV. The angle of ejection was 90° to the incident electron direction. The incident electron energy was 2.0 keV.

Figures 5.1.1(b) and 5.1.1(c) show values of the DDCS(n+) and the DDCS plotted against secondary electron energy for incident electron energies of 1.0 keV and 2.0 keV respectively. The values of the DDCS have been normalised to the similar results by Opal et al. (1972), at 100 eV secondary electron energy. Theoretical values of the DDCS using the plane wave Born approximation (PWBA) (Bell and Kingston, 1975) are also shown. A common feature that can be noticed is that the curves showing the present results of the DDCS fall less rapidly than those showing results of Opal et al., 1972. Another feature that is evident in figure 5.1.1(c) is a small peak in the curves for the DDCS and DDCS(1+) at 35 eV, secondary electron energy, which is due, perhaps, to the autoionization of doubly excited He (Gibson and Reid, 1986). In figure 5.1.1(c), values of DDCS(2+) show a broad peak at 100 eV secondary electron energy.

Figure 5.1.1(d) shows relative values of the DDCS(n+) for helium ions in coincidence with electrons of 200 eV secondary electron energy, plotted against incident electron energy.

5.1.2 Argon

Figure 5.1.2(a) shows a TOF spectrum for argon ions in coincidence with secondary electrons of 200 eV energy when the incident electron energy was 1.5 keV. Angle of ejection was 90°. Peaks for Ar^+, Ar^{2+}, Ar^{3+} and Ar^{4+} can be seen.

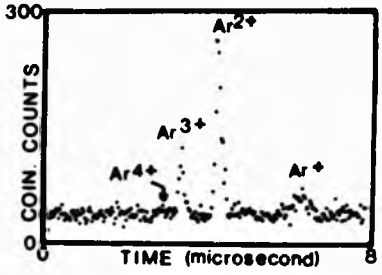

Figure 5.1.2(a): TOF spectrum for argon.

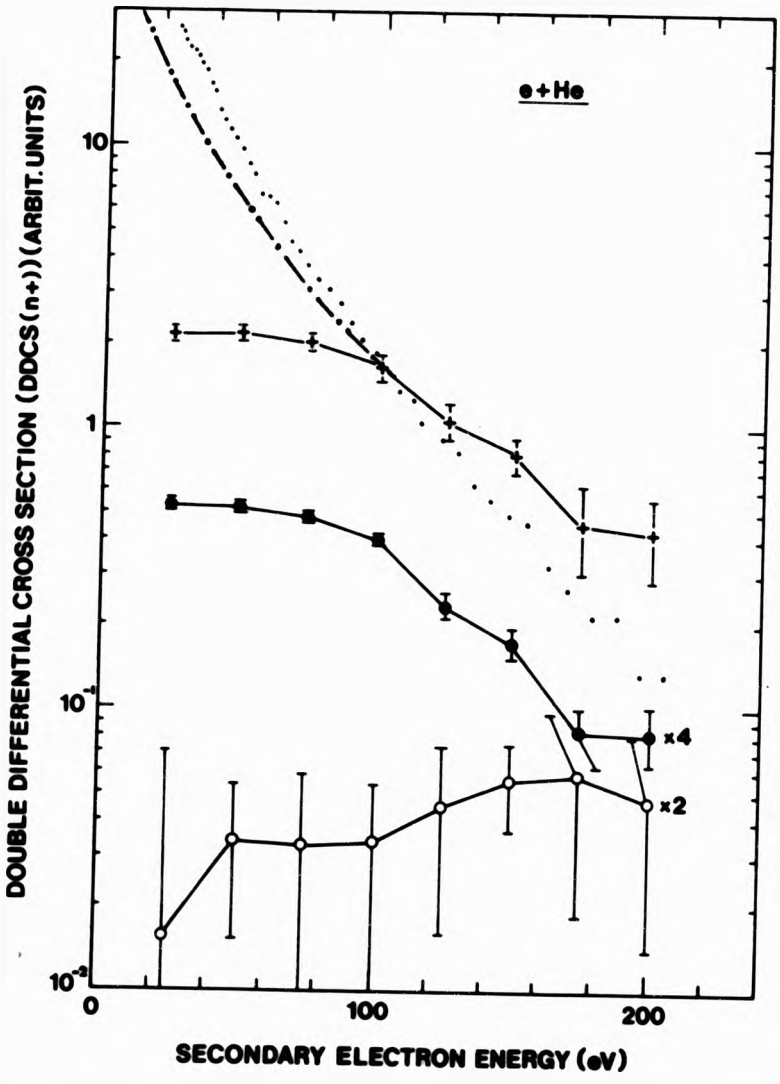

Figure 5.1.1(b): DDCS(n+) plotted against secondary electron energy. DDCS(n+) measurements are denoted ●He^{+} , oHe^{2+}. Also shown are the present DDCS marked + and the results of Opal et al., 1972 (.....). Incident electron energy is 1.0 keV. The values for DDCS(1+) shown represent the observed values divided by 4 and those for DDCS(2+) the observed values divided by 2. Line -·-·- shows the theoretical values of Bell and Kingston (1975).

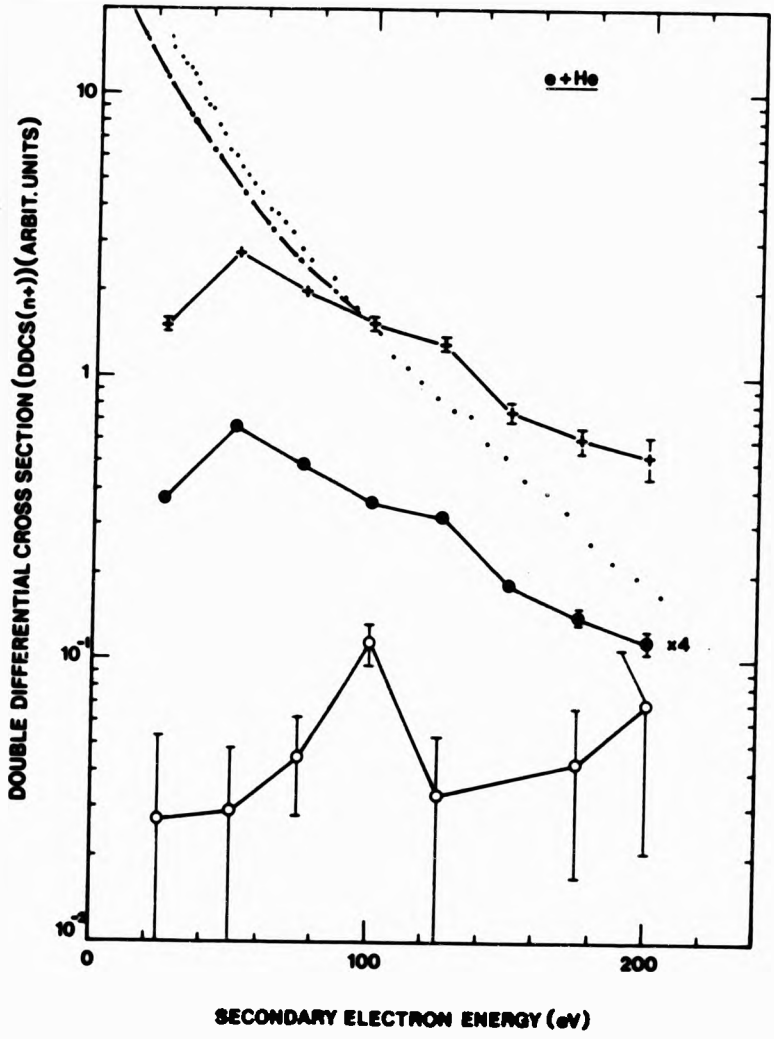

Figure 5.1.1(c): Relative values of DDCS(n+) and DDCS plotted against secondary electron energy, incident electron energy being 2.0 keV. Present results for DDCS marked + were normalised to the results of Opal et al. (1972) (....) at 100 eV secondary electron energy. Present measurements are for $^{\bullet}He^{+}$ and $^{\circ}He^{2+}$. The values of DDCS(1+) represent the observed values divided by 4.
Lines are to guide the eye.
Line -·-·- shows the theoretical values of Bell and Kingston (1975).

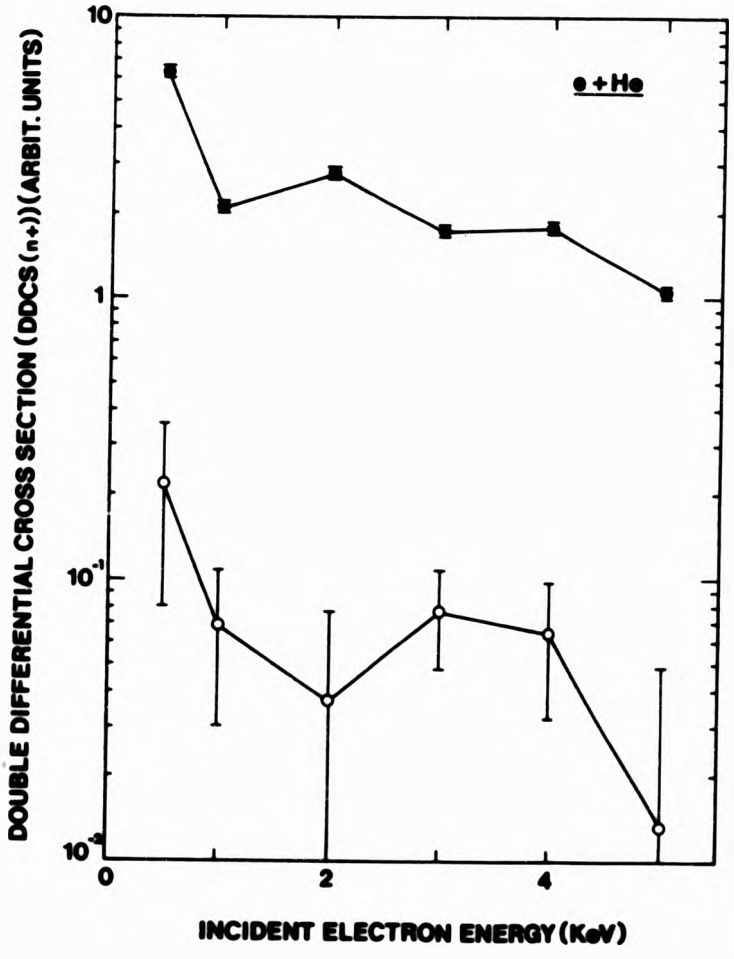

Figure 5.1.1(d): DDCS(n+) plotted against incident electron energy for secondary electron energy of 200 eV. Measurements are for ●He^{+} and oHe^{2+}.

Figures 5.1.2(b), 5.1.2(c) (i) and 5.1.2(d) show relative values of the DDCS(n+) and the DDCS plotted against secondary electron energy for incident electron energies of 1.0 keV, 1.5 keV and 2.0 keV. The DDCS(1+) results chiefly from the removal of outer shell electrons, i.e. 3p electrons, as the probability of ionizing the 3s electrons is only 1% (Luyken et al., 1972). Multiply charged ions can result from direct multiple ionization or from inner-shell ionization followed by Auger transitions (such as LMM transitions) and shake-off (Carlson and Nester, 1973) processes. The DDCS(2+) values show prominent peaks at 200 eV, secondary electron energy, due to the strong LMM Auger transitions in this region. The DDCS(3+) values also exhibit similar peaks but at about 20 eV lower secondary electron energy (Hippler et al., 1984a) The DDCS(2+) and DDCS(3+) also show a broad peak at 40 eV which could be due to Coster-Kronig transitions (Mehlhorn, 1968). Figure 5.1.2(c)(ii) shows the variation of mean charge $\bar{n}(E)$ with secondary electron energy. It is evident that low energy secondary electrons are mostly associated with single ionization while electrons around 200 eV are mostly associated with multiply charged ions and $\bar{n}(E)$ has values higher than two. In fact the peak at 185 eV due to LMM transition is quite evident here.

Figure 5.1.2(e) shows relative values of the DDCS plotted against secondary electron energy for incident electron energies of 1.0 keV, 1.5 keV and 2.0 keV. Similar results obtained by Opal et al. (1972) for 500 eV, incident electron energy, are also shown for comparison. Present results agree generally with the results of Opal et al. (1972) in spite of the difference in incident electron energies.

Figure 5.1.2(b). Relative values of the DDCS(n+) and the DDCS plotted against secondary electron energy, incident electron energy being 1.0 keV. Measurements are denoted $\bullet Ar^{+}$, $\circ Ar^{2+}$, $\blacktriangle Ar^{3}$. The DDCS is marked +. Values of DDCS(2+), DDCS(3+) and DDCS have been divided by 20, 100 and $\frac{1}{2}$ respectively for better presentation.

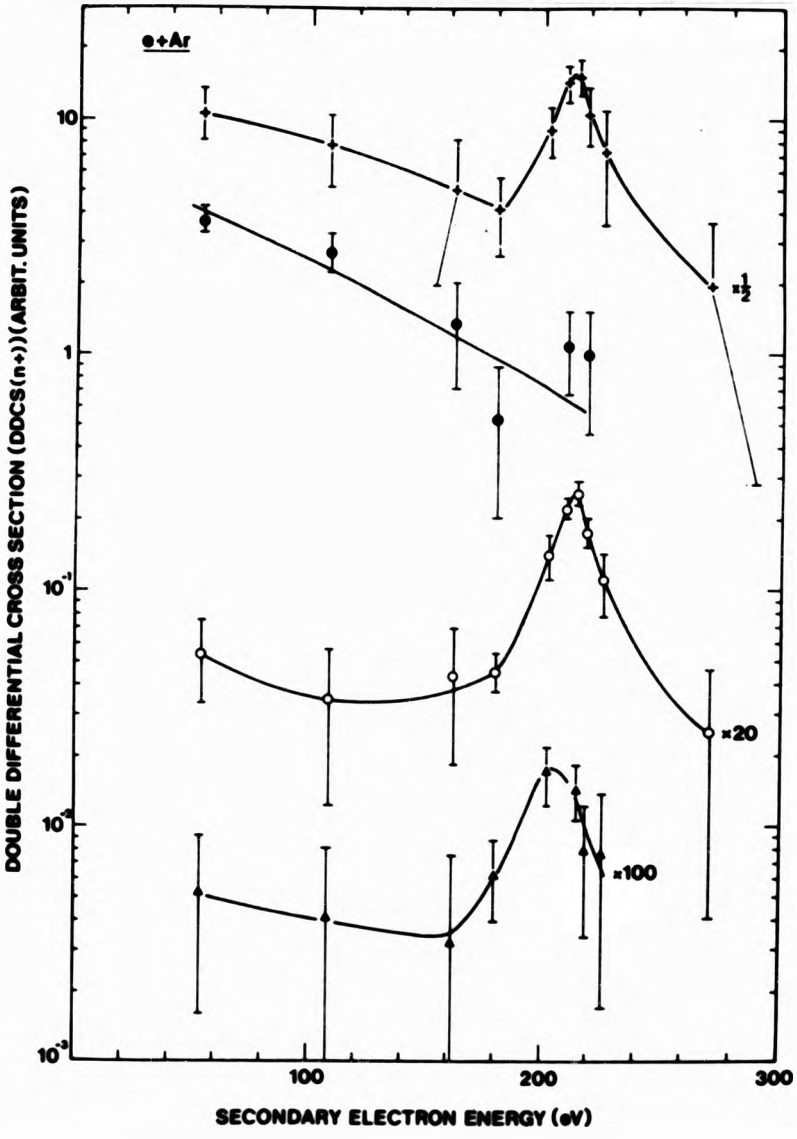

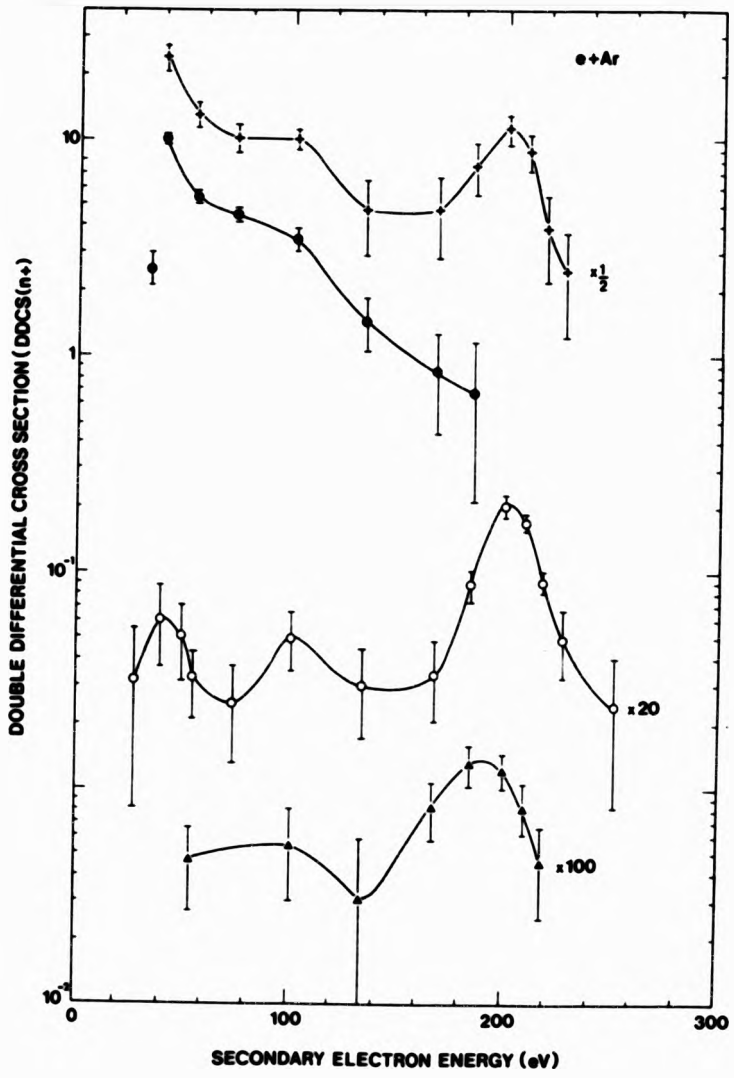

Figure 5.1.2(c). Relative values of DDCS(n+) and DDCS plotted against secondary electron energy, incident electron energy being 1.5 keV. Measurements are denoted ●Ar^+, ○Ar^{2+}, ▲Ar^{3+}. The DDCS is marked +. Lines are to guide the eye.

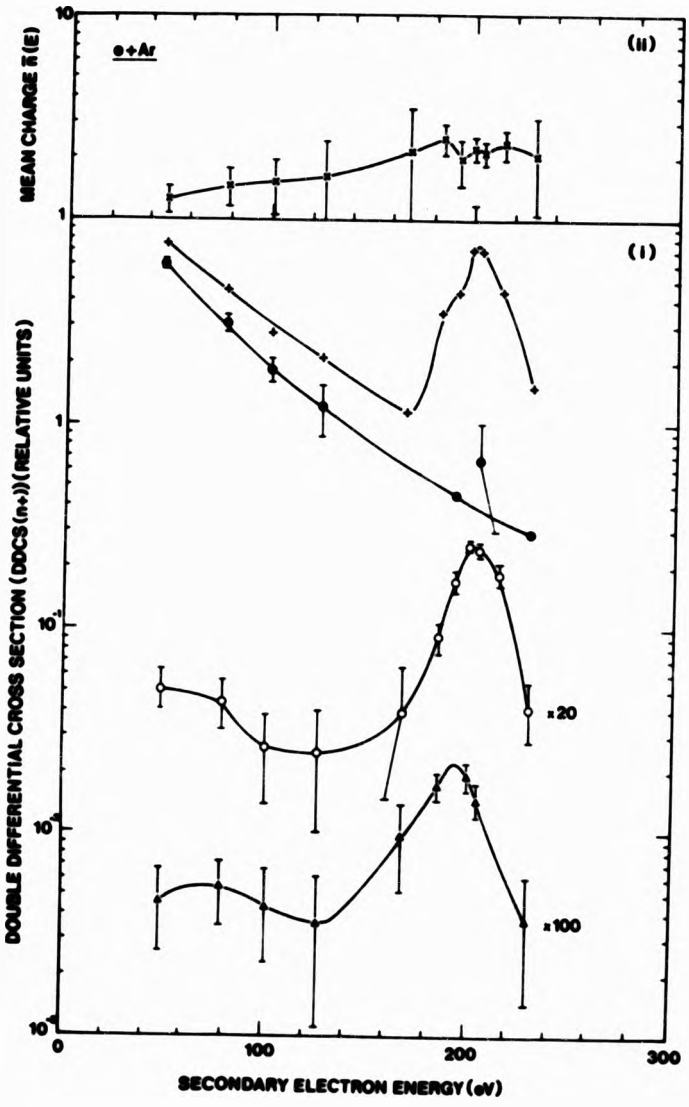

Figure 5.1.2(d)(i). Values of DDCS(n+) plotted against secondary electron energy, incident electron energy being 2.0 keV. Measurements are denoted $\bullet Ar^{+}$, $\circ Ar^{2+}$, $\blacktriangle Ar^{3+}$. The DDCS is marked +. Lines are to guide the eye.

Figure 5.1.2(d)(ii). Values of mean charge $\bar{n}(E)$ plotted against secondary electron energy.

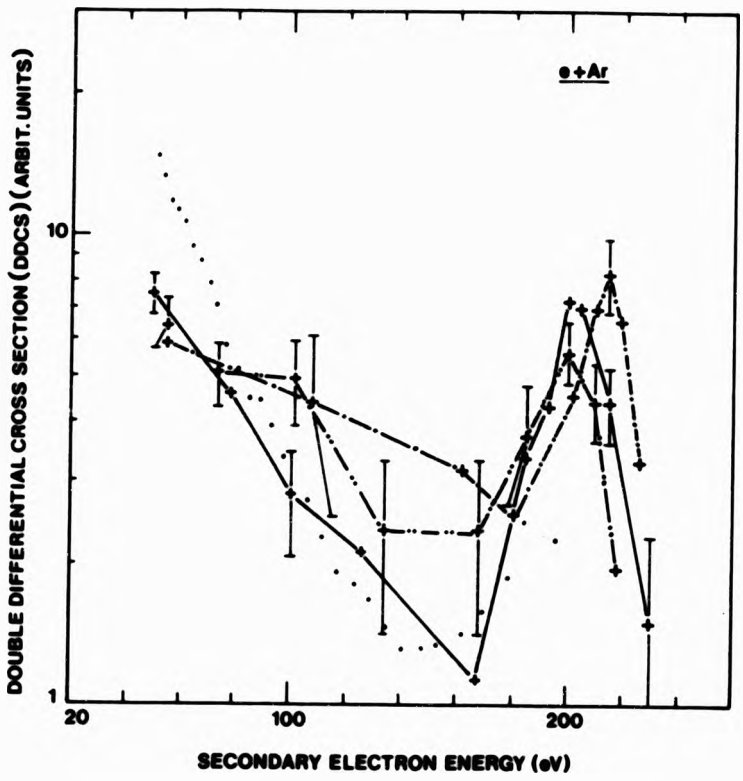

Fig. 5.1.2(e) DDCS values drawn against secondary electron energy for incident electron energies of (——) 2.0 keV, (-•••-) 1.5 keV and (•••) 1.0 keV. (••••) shows the similar results of Opal et al. (1972) for an incident electron energy of 500 eV. Only 2.0 keV values were normalised at 100 eV to their results.

Figure 5.1.2(f) shows the relative values of DDCS(n+) plotted against incident electron energy for secondary electron of 200 eV energy. At this ejected electron energy multiple ionization results mainly from L-shell ionization, whereas singly charged ions result from M-shell ionization. According to Krause (1979), 93.4% of the vacancies in the L_1-subshell can decay by Coster-Kronig transitions resulting in L_2 or L_3 vacancies. These L_2 or L_3 vacancies

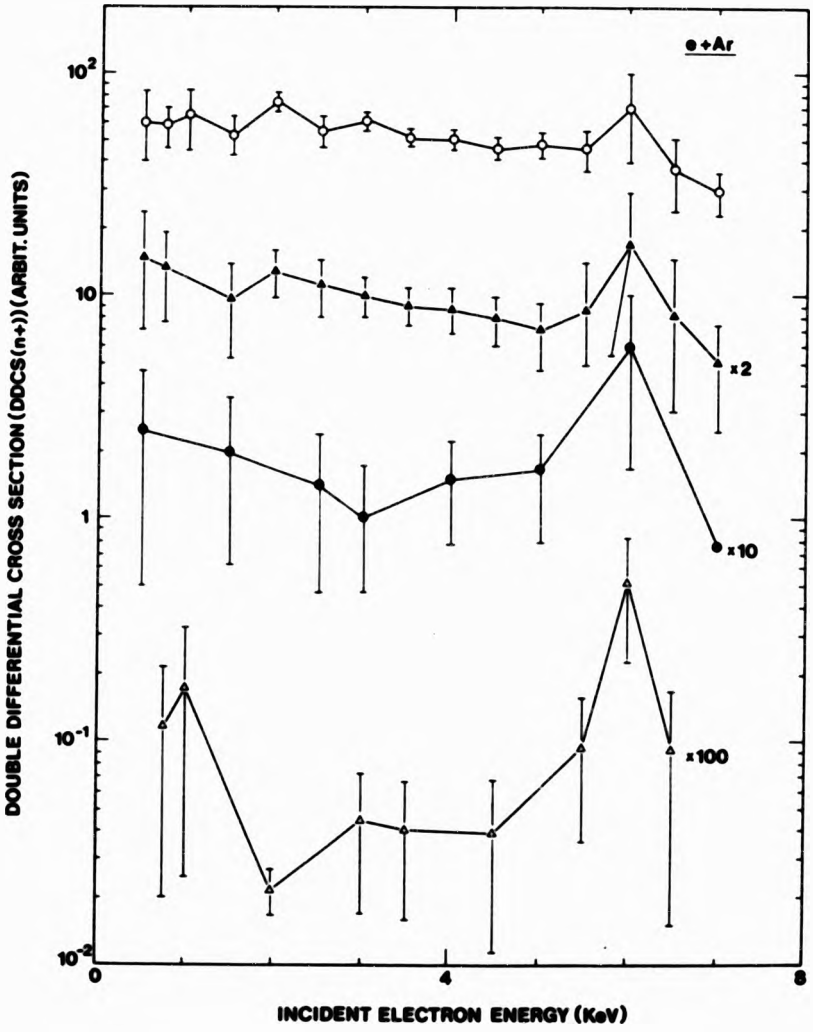

Figure 5.1.2(f). Values of the DDCS plotted against incident electron energy for 200 eV secondary electron energy. Measurements are for $\bullet Ar^{+}$, $\circ Ar^{2+}$, $\blacktriangle Ar^{3+}$ and $\triangle Ar^{4+}$. The lines are to guide the eye.

then, almost exclusively, decay via Auger electron emission. In addition, shake-off processes following L-vacancy production, have a probability of occurrence of about 15% (Carlson and Nester, 1973). The calculated values of $\sigma(L)$ (Hippler et al., 1984b) for the production of different charge states after the creation of L-vacancies, are compared with the present results for an incident electron energy of 2.0 keV in table 5.1.2(1). The results of Stolterfoht et al. (1973) are also given

Table 5.1.2(1)

Charge state	Present results	$\sigma(L)$	Stolterfoht et al.(1973)
2+	72.5	70.7	54
3+	25.2	26.8	44
4+	2.3	2.5	2

Figure 5.1.2(g) shows the values of the DDCS(n+) plotted against incident electron energy for a secondary electron energy of 200 eV. Assuming that Auger emission is isotropic and neglecting direct-double ionization of M-shell, the DDCS(2+) and DDCS(3+) are given by (Van der Wiel and Wiebes, 1971; Hippler et al., 1984b)

$$DDCS(2+) = 0.89\sigma(L_{2,3}) , \qquad 5.1.2\text{-}1$$

$$DDCS(3+) = 0.84\sigma(L_1) + 0.92\sigma(L_{2,3})S , \qquad 5.1.2\text{-}2$$

where S is the shake-off probability following L-shell ionization. Equation (5.1.2-1) gives good agreement with the DDCS(2+) data except at energies below 2.0 keV (Hippler et al. 1984b), and equation 5.1.2-2 with S = 0 also agrees fairly well with the present data.

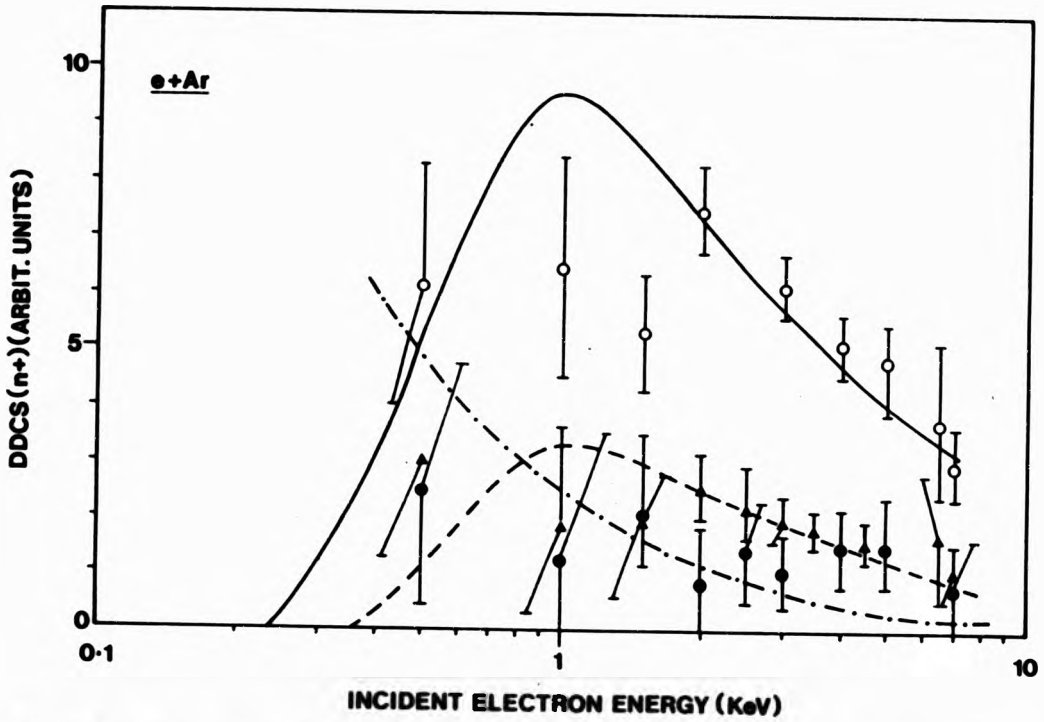

Figure 5.1.2(g). Values of DDCS(n+) are plotted against incident electron energy, secondary electron energy being 200 eV. Present measurements are for $\bullet Ar^{+}$, $\circ Ar^{2+}$, $\blacktriangle Ar^{3+}$. Solid and dashed lines represent the L-shell contribution with S = 0 to DDCS(2+) and DDCS(3+) respectively. The dashed-dotted line is a singly differential cross section for M-shell ionization.

5.1.3 Krypton

Figure 5.2.3(a) shows a TOF spectrum for krypton ions detected in coincidence with secondary electrons of 85 eV energy, incident electron energy being 10.0 keV. Peaks for ions having charge states 1+ to 6+ can be seen. As krypton gas has several isotopes, each peak is a sum of several closely spaced peaks, one for every isotope (Short et al., 1986). The inset in the figure shows the peak for Kr^{2+} more closely and separate peaks for each isotope can be seen.

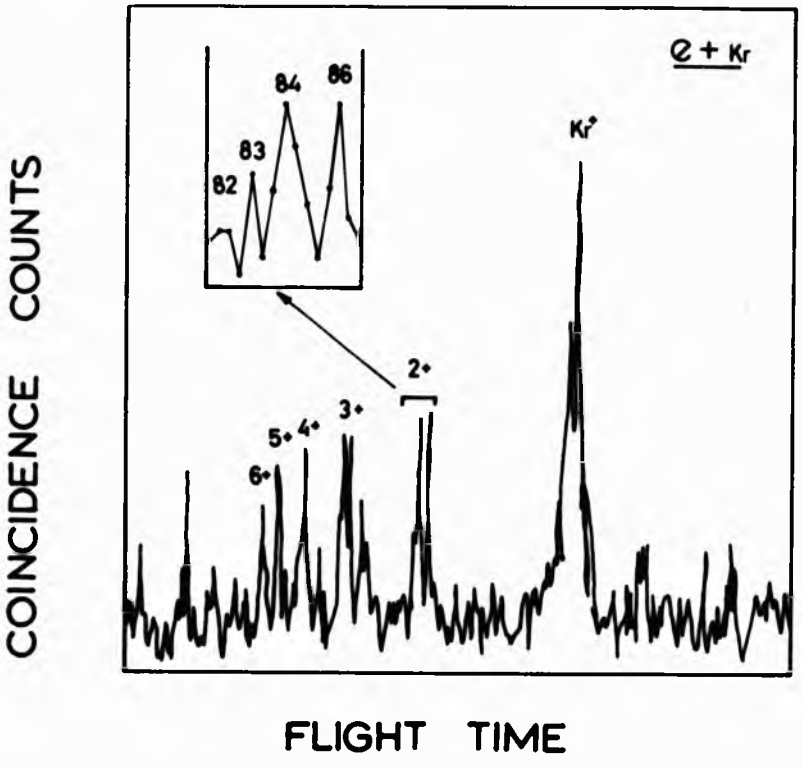

Figure 5.1.3(a). TOF spectrum for krypton. The inset shows the isotopic spread of the peak for the Kr^{2+} ion.

Figure 5.1.3(b) shows similar TOF spectra for different secondary electron energies, the incident electron energy being the same. This demonstrates the variation in the relative strength of the

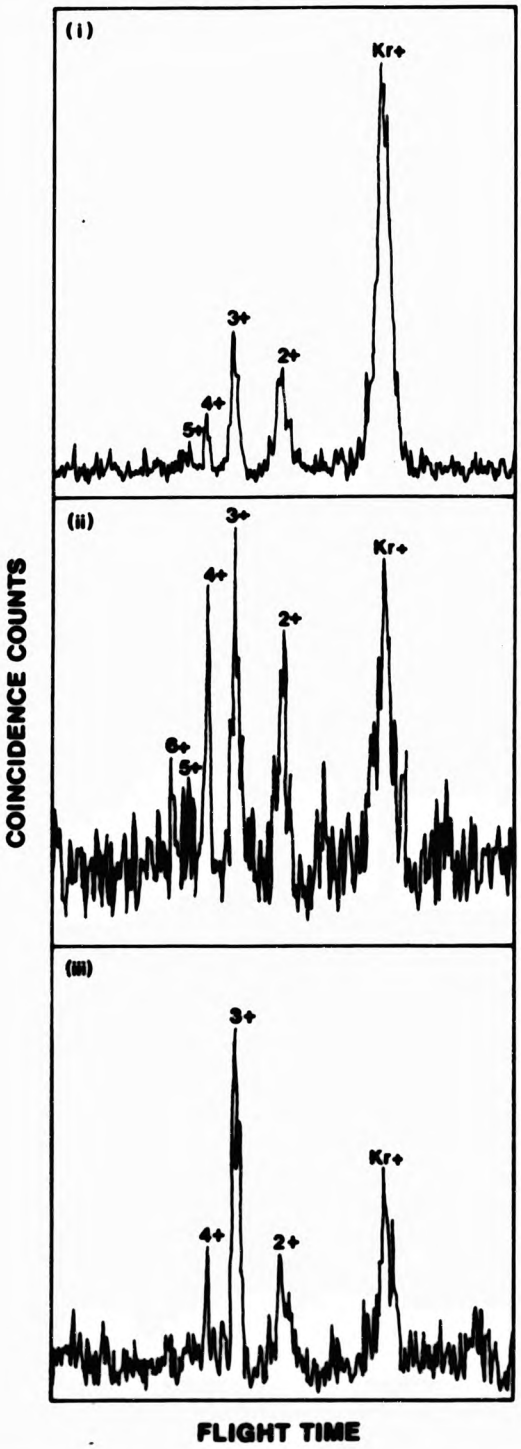

Figure 5.1.3(b)

TOF spectra for krypton ions for secondary electron energies of

(i) 15 eV

(ii) 63.5 eV

(iii) 70.0 eV.

The incident electron energy was 10.0 keV.

peaks for ions of different charge states as the energy of the accompanying secondary electron changes.

Figure 5.1.3(c) shows relative values of the DDCS(n+) and DDCS plotted against secondary electron energy. The incident electron energy is 10.0 keV and the angle of ejection is 90°. Present values of DDCS are found to agree generally with similar results of Opal et al. (1972) for incident electron energies of 500 eV. The small disagreement could well be due to the difference in incident electron energies. The shape of the DDCS curve is also found to agree with the results of Oda et al. (1972) (not shown in the figure). The following features can also be noted about the DDCS(n+) values.

(i) the DDCS(2+) has relatively higher values at lower secondary electron energies except around 200 eV, where it shows an increase. Prominent peaks can also be seen in the regions of the Coster-Kronig transitions LLM, MMN and the Auger transitions MNN.

(ii) the DDCS(3+) has its highest value at the lowest energy measured for the detected electron. It shows a monotonic decrease with detected electron energy except for the peaks near the strong transitions such as $L_1L_3M_{4,5}$, $M_1M_{4,5}M_{4,5}$ and $M_{2,3}M_{4,5}N_{2,3}$.

(iii) the DDCS(4+) also shows higher values at lower secondary electron energies. There is a prominent peak around 70 eV which is about 15 eV lower than the corresponding peak in the DDCS(3+). This agrees with the results of Hippler et al. (1984a) who found a shift of 20 eV per charge state in similar peaks.

Figure 5.13(d) shows relative values of the DDCS(n+) plotted against incident electron energy, secondary electron energy being 60 eV. The DDCS(n+) generally show changes in their values at L-subshell ionization potentials. The DDCS(5+) shows a prominent peak at

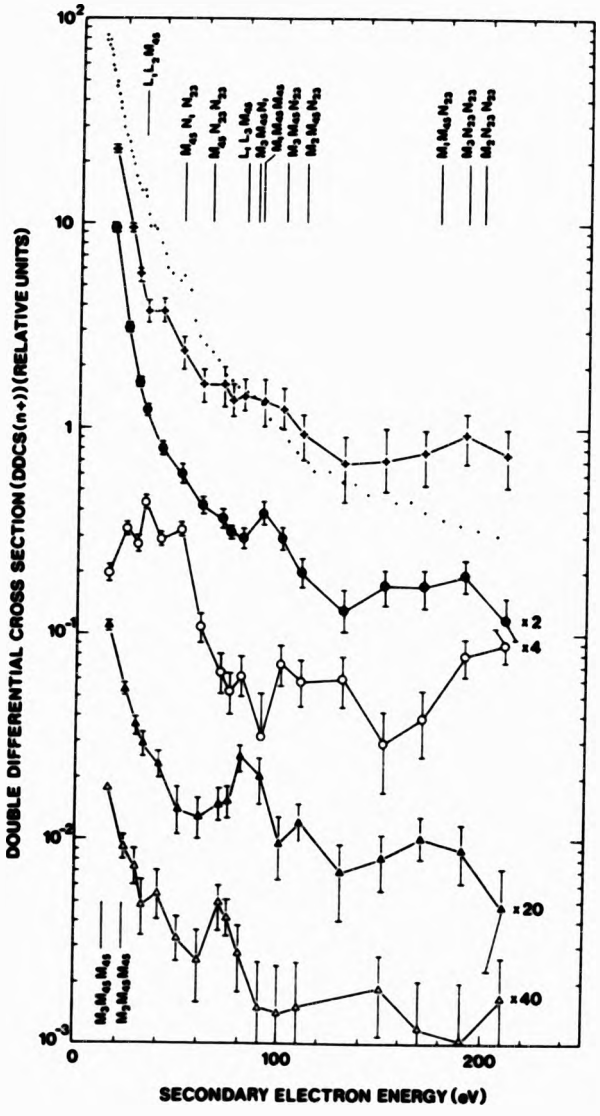

Figure 5.1.3(c). Relative values of the DDCS(n+) plotted against secondary electron energy, the incident electron energy being 10.0 keV. Measurements are for ●Kr^{+}, ○Kr^{2+}, ▲Kr^{3+}, △Kr^{4+}. The DDCS are marked +. The line ..... show the experimental results of Opal et al. (1972). The present values of the DDCS were normalised to the data of Opal et al. (1972) at 85 eV, secondary electron energy.

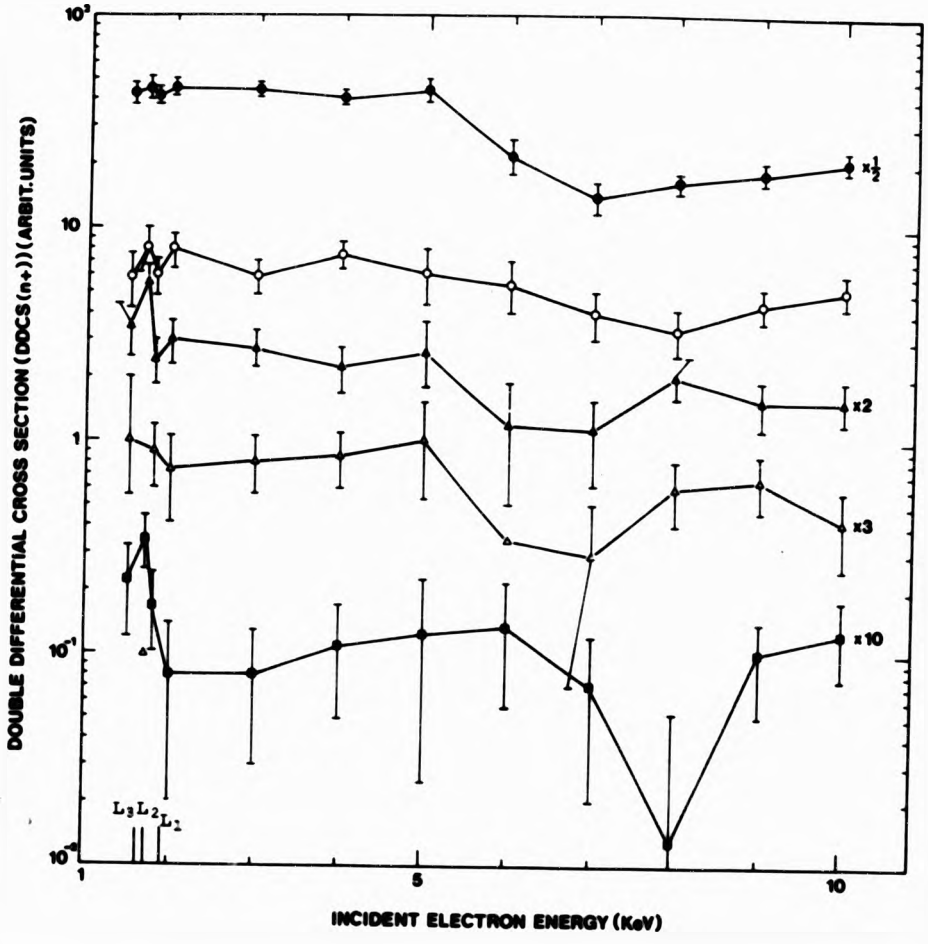

Figure 5.1.3(d). DDCS(n+) plotted against secondary electron energy, incident electron energy being 10.0 keV. Measurements are for Kr^{+}, Kr^{2+}, Kr^{3+}, Kr^{4+} and Kr^{5+}.

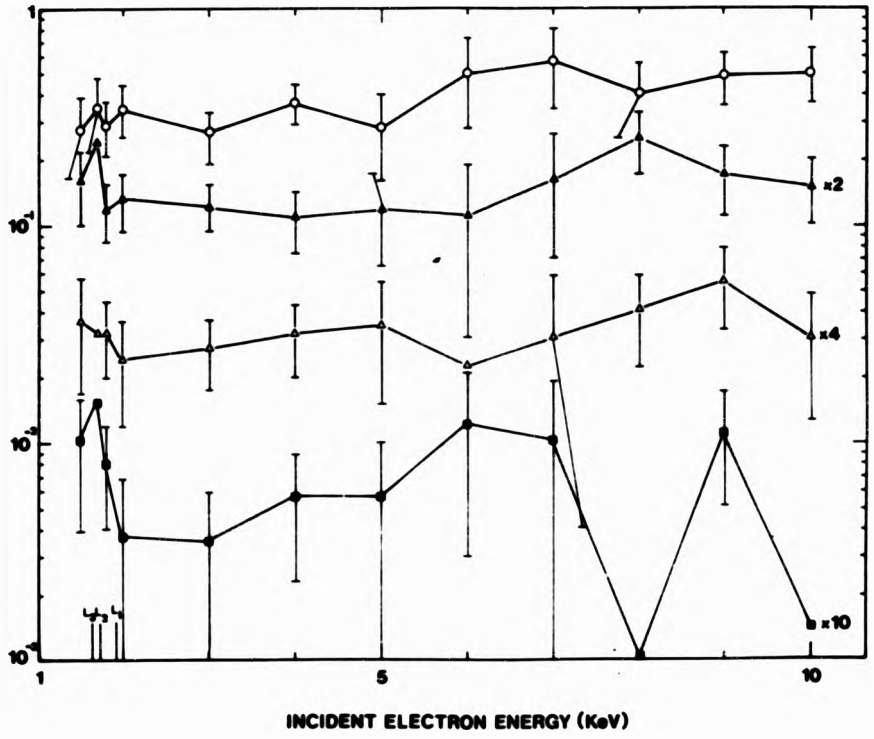

Figure 5.1.3(e)

The ratio DDCS(n+),DDCS(1+) plotted against incident electron energy, secondary electron energy being 60 eV. Measurements are for ●Kr^{+}, ○Kr^{2+}, ▲Kr^{3+}, △Kr^{4+} and ■Kr^{5+}.

the $L_{2,3}$-subshell ionization potentials.

Figure 5.1.3(e) shows values of DDCS(n+)/DDCS(1+), from the data of figure 5.1.3(d), plotted against the incident electron energy. The variations in the values of the ratios, DDCS(n+)/DDCS(1+), at L-subshell edges are evident.

5.1.4 Xenon

Figure 5.1.4(a) shows a TOF spectrum for xenon ions detected in coincidence with secondary electrons of 30 eV energy at an incident electron energy of 6.0 keV. Peaks for xenon ions having charge states from 1+ to 9+ can be seen. The width of the peaks is due mainly to the isotopic spread (§5.1.4) of xenon ions, the contribution due to the thermal energy spread of the gas atoms being much less in comparison (Short et al. 1986). The asymmetry in the shape of the peaks is due to the mass distribution of isotopic abundance in xenon atoms.

Figure 5.1.4(b)/(i) shows the relative values of the DDCS(n+) and the DDCS plotted against secondary electron energy, incident electron energy being 6.0 keV. The DDCS generally exhibits a smooth decrease (Oda et al., 1972; Opal et al, 1972; Ogurtsov, 1973) with increase in the energy of the emitted electrons. Electrons ejected from auto-ionization states have definite sharp energies and the corresponding spectrum is superimposed due to direct ionization and double Auger (Mehlhorn, 1985) transitions such as $N_{45}OOO$ which accounts for 27% of the total radiationless transition rate (Cairns, 1969) from N_{45} subshells. The sharp increase in the DDCS corresponds to the Auger transition $N_{45}O_1O_{23}$ (McGuire, 1982) emitting 32.8 eV electrons. Figure 5.1.4(b)/(i) also shows that the present results for the DDCS agree

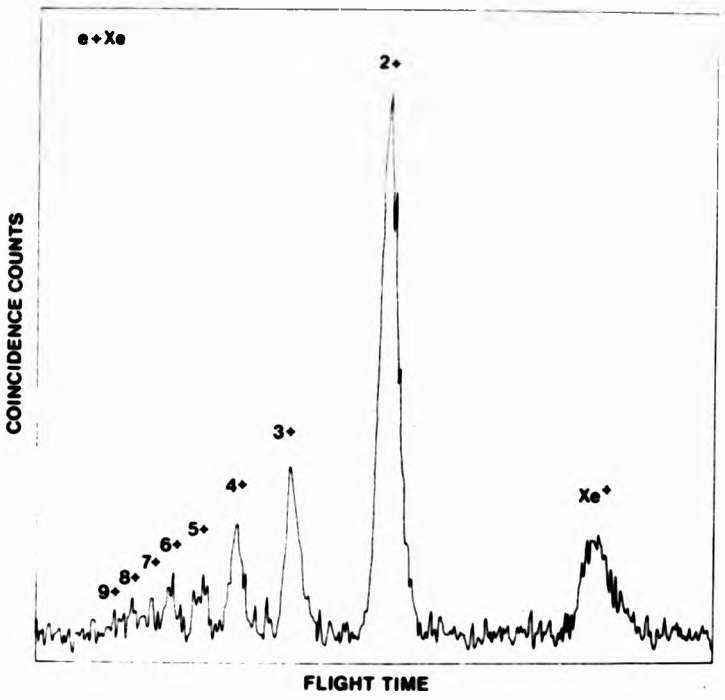

Figure 5.1.4(a). Time-of-flight (TOF) spectrum of xenon ions formed as a result of electron impact on xenon atoms. Incident electron energy and ejected electron energy were 6.0 keV and 30 eV respectively. Ejection angle was 90°. Peaks for Xe^{+} to Xe^{9+} can be seen.

generally with similar results of Opal et al. (1972) for 500 eV incident electron energy. At secondary electron energies greater than 100 eV, however, the values for the DDCS are higher than those of Opal et al. (1972). This increase could be due to the several additional single (Coghlan and Clausing, 1973) and double (Mehlhorn, 1985) Auger transitions which are possible at 6.0 keV incident electron energy.

Figure 5.1.4(b)/(ii) shows the mean charge $\bar{n}(E)$ as a function of the secondary electron energy E. The higher mean charge values around 40 eV are due perhaps to the strong $N_{45}O_1O_{23}$ Auger transitions (Coghlan and Clausing, 1973) in this region. As a result, perhaps, of the

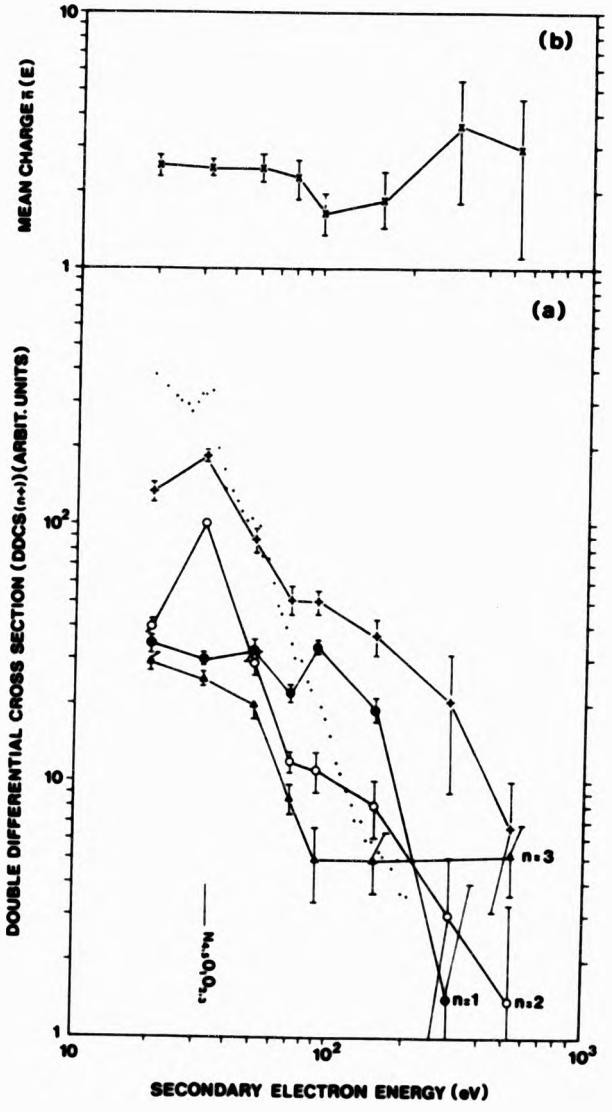

Figure 5.1.4(b). (i) Relative values of the DDCS(n+) and DDCS plotted against secondary electron energy, the incident electron energy being 6.0 keV. Measurement are for $\bullet Xe^{+}$, $\circ Xe^{2+}$ and $\blacktriangle Xe^{3+}$, The DDCS are marked +. The line ..... shows the results of Opal et al. (1972) for the DDCS at 500 eV, incident electron energy.
(ii) Values of mean charge n(E) plotted against secondary electron energy.

absence of Auger electrons in the region of 100 eV secondary electron energy, the value of $\bar{n}(E)$ shows a minimum at this energy.

Figure 5.1.4(c) shows relative values of the DDCS(n+) for n=1 to 8 plotted against the incident electron energy for an ejected electron energy of 30 eV and an ejection angle of 90°. Higher order ionization is mainly produced by the removal of innershell electrons followed by a vacancy cascade, but, for multiple ionization to be detected in our experiment, the vacancy cascade must end at N_{45} subshells or should otherwise eject an electron of 30 eV by some other process. A vacancy in the L_1-subshell, for example, has a 52.4% possibility (Chen et al., 1981) of being transferred to the L_{23} subshells by a Coster-Kronig transition which could be followed by several Auger/Coster-Kronig transitions (Coghlan and Clausing, 1973) such as $L_3M_3M_3$, $M_3M_5O_{45}$) $M_5N_{45}N_{45}$, and $N_{45}O_1O_{23}$, resulting in the ejection of up to five or more electrons. If one adds to this the contributions due to shake-off (Carlson and Nester, 1973) processes as well, the high state of ionization reached in these processes is quite understandable. Figure 5.1.4(c)(i) also shows that, at incident electron energies higher than M-shell ionization potentials, the DDCS(n+) for all charges show an increase in their values. The DDCS(2+) and DDCS(4+) have peaks at 4.0 keV, while the DDCS(3+) has a peak at 3.0 keV incident electron energy. The DDCS(2+), DDCS(3+) and DDCS(4+) show jumps in their values at the L-subshell edges. A trend towards production of ions with higher charges beyond 7.0 keV incident electron energy is also evident. This observation agrees generally with the results of photoionization studies (Short et al., 1986; Carlson et al., 1966) showing that vacancies in the L-shell can result in a higher average charge per ion than vacancies in the M-shell or N-shell.

Figure 5.1.4(c)(ii) shows values of $\bar{n}(E)$ for E = 30 eV plotted against incident electron energy, and reveals that there is a relative

Figure 5.1.4(c)

(i) Relative values of DDCS(n+) and DDCS plotted against incident electron energy, secondary electron energy being 30 eV. Measurements are for $\bullet Xe^{+}$, $\circ Xe^{2+}$, $\blacktriangle Xe^{3+}$, $\triangle Xe^{4+}$, $\blacksquare Xe^{5+}$, $\square Xe^{6+}$, $\blacktriangledown Xe^{7+}$ and $\triangledown Xe^{8+}$.

(ii) Values of mean charge $\bar{n}(E)$ plotted against incident electron energy

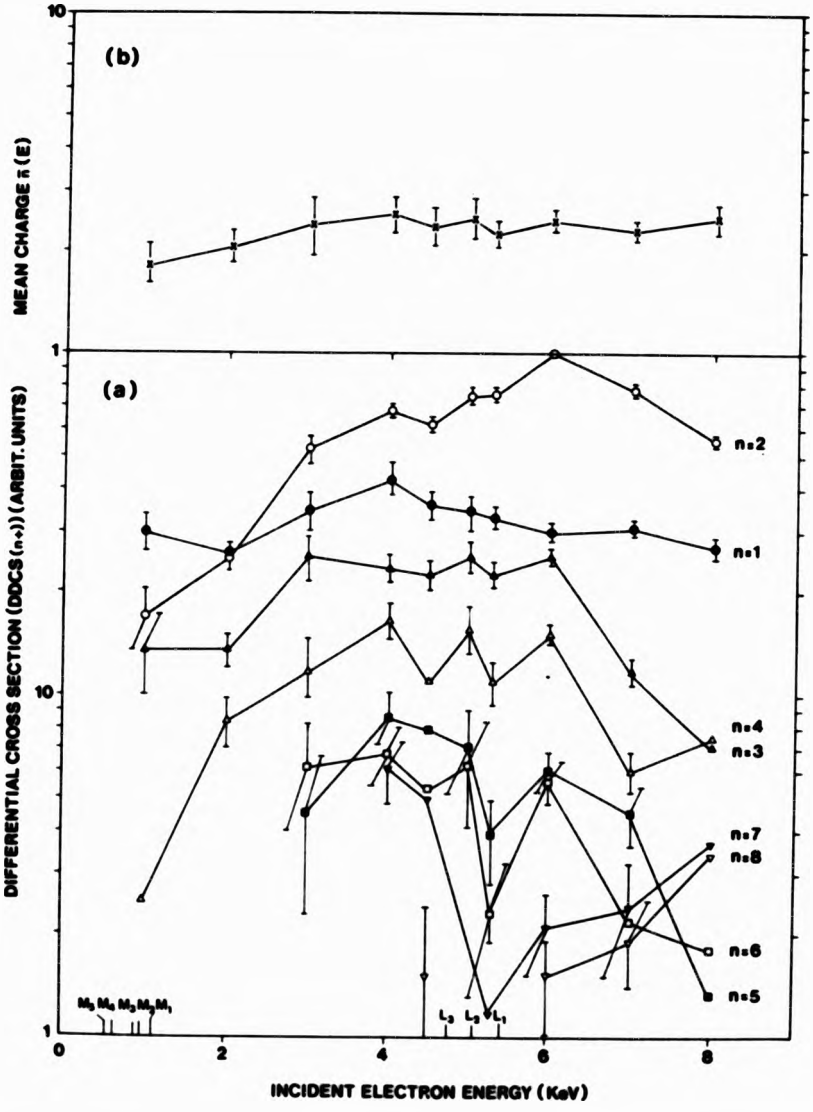

increase in production of ions with higher charges at incident electron energies greater than 1.0 keV. Jumps in the value of $\bar{n}(E)$ for energies just above the L-subshell edges are also evident.

5.1.5 Neon

Figure 5.1.5(a) shows a TOF spectrum for neon ions detected in coincidence with secondary electrons of 200 eV energy, incident electron energy was 3.0 keV. Neon consists of two isotopes ^{20}Ne and ^{22}Ne having 90.9% and 8.8% abundances respectively. There is a 10% difference in their masses which is much larger than the mass resolution of the ion-analyser, therefore, the peaks for each charge state show a break up into two separate peaks. The spectrum shows peaks for $^{22}Ne^{+}$, $^{20}Ne^{+}$, $^{22}Ne^{2+}$, $^{20}Ne^{2+}$, $^{20}Ne^{3+}$ and $^{20}Ne^{6+}$. For higher charge states the peaks become smaller and for ^{22}Ne isotope, being less abundant, become too small to be identified. The peak for Ne^{+} is most prominant. The ratio for DDCS(2+)/DDCS(1+) has been estimated to be 0.055 (∿ 40% error).

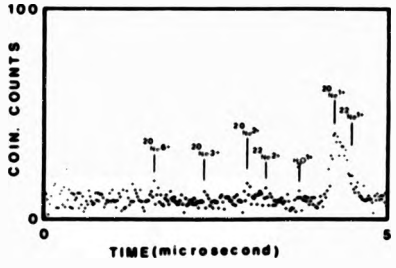

Figure 5.1.5(a). TOF spectrum for neon ions detected in coincidence with secondary electrons of 200 eV. Incident electron energy was 3.0 keV.

5.2 X-ray-ion coincidence experiment

Figure 4.2(a) shows the experimental arrangement for the x-ray-ion coincidence experiment carried out for xenon atoms under electron impact. In this experiment xenon ions produced as a result of ionization were detected in coincidence with the x-rays emitted by the ion at 90° to the incident electron direction. The x-rays were detected by a liquid nitrogen cooled HPGe detector and the ions were analysed, in respect of their charge state by a TOF type analyser 3.5(a). Figure 4.2(b) shows the electronic circuit used to record coincidences between the detected ions and x-rays. Figure 5.2(a) shows such a TOF spectrum for xenon as a result of the impact of electrons having 11.0 keV energy. The TOF spectrum shown in Figure 5.2(a) has been used to find the relative

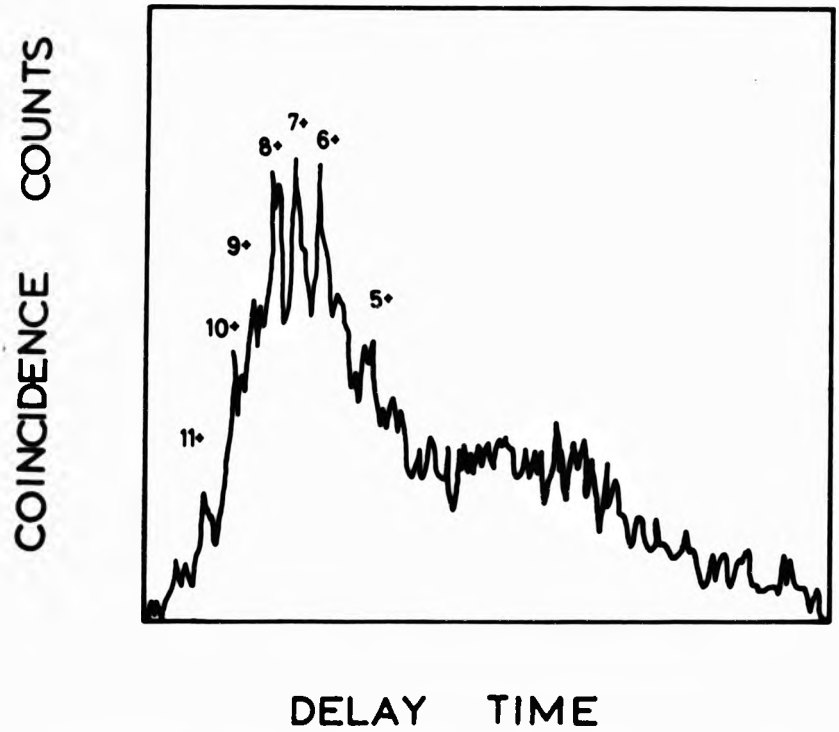

Figure 5.2(a) TOF spectrum of xenon ions detected in coincidence with x-rays emitted at 90° to the incident electron direction. The incident electron energy is 11.0 keV.

abundances of xenon ions, having different charge states, which were detected in coincidence with the emitted x-rays. Figure 5.2(b) shows that Xe^{8+} has the highest intensity amongst the detected ions. Present results yield an average charge per ion, detected in coincidence with the emitted x-rays, of 6.9. This distribution of charge state can result (Carlson et al. 1966; Short et al. 1986) from L-shell ionization followed by Coster-Kronig transition (Chen et al. 1981), a radiative transition and several possible Auger transitions (Coghlan and Clausing, 1973). The contribution of shake-off process towards increasing the state of ionization may also not be negligible (Carlson and Nester, 1973).

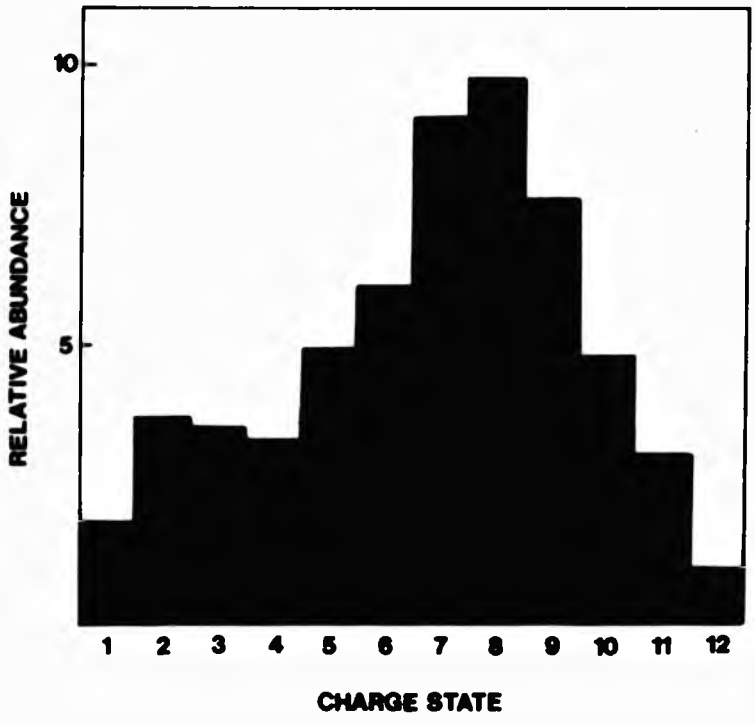

Figure 5.2(b) Relative abundance of xenon ions, detected in coincidence with x-rays emitted at 90° to the incident electron direction, as a function of the charge state of the ion. Incident electron energy was 11.0 keV.

5.3 X-ray spectroscopy using crystal x-ray spectrometer

Figure 5.3(a) shows a second order spectrum of the K_α and K_β lines of ^{54}Mn taken by using a Nacℓ(100) crystal. These x-rays are emitted by a ^{55}Fe radioactive source as a result of electron capture (EC) (Hatch, 1964 and Schnopper, 1966). The experimental arrangement and the electronic set up is given in section 4.3. From Figure 5.3(a) the spectrometer resolution for the K_α line is found to be 161 eV.

A comparison between Figure 5.3(a) and figure 5.3(b) shows that the crystal x-ray spectrometer has over ten times better resolution than the HPGe detector (Wille and Hippler, 1986). This crystal x-ray spectrometer can, therefore, be used in x-ray spectroscopy in the keV energy range with considerable advantage, provided sufficient intensity is available.

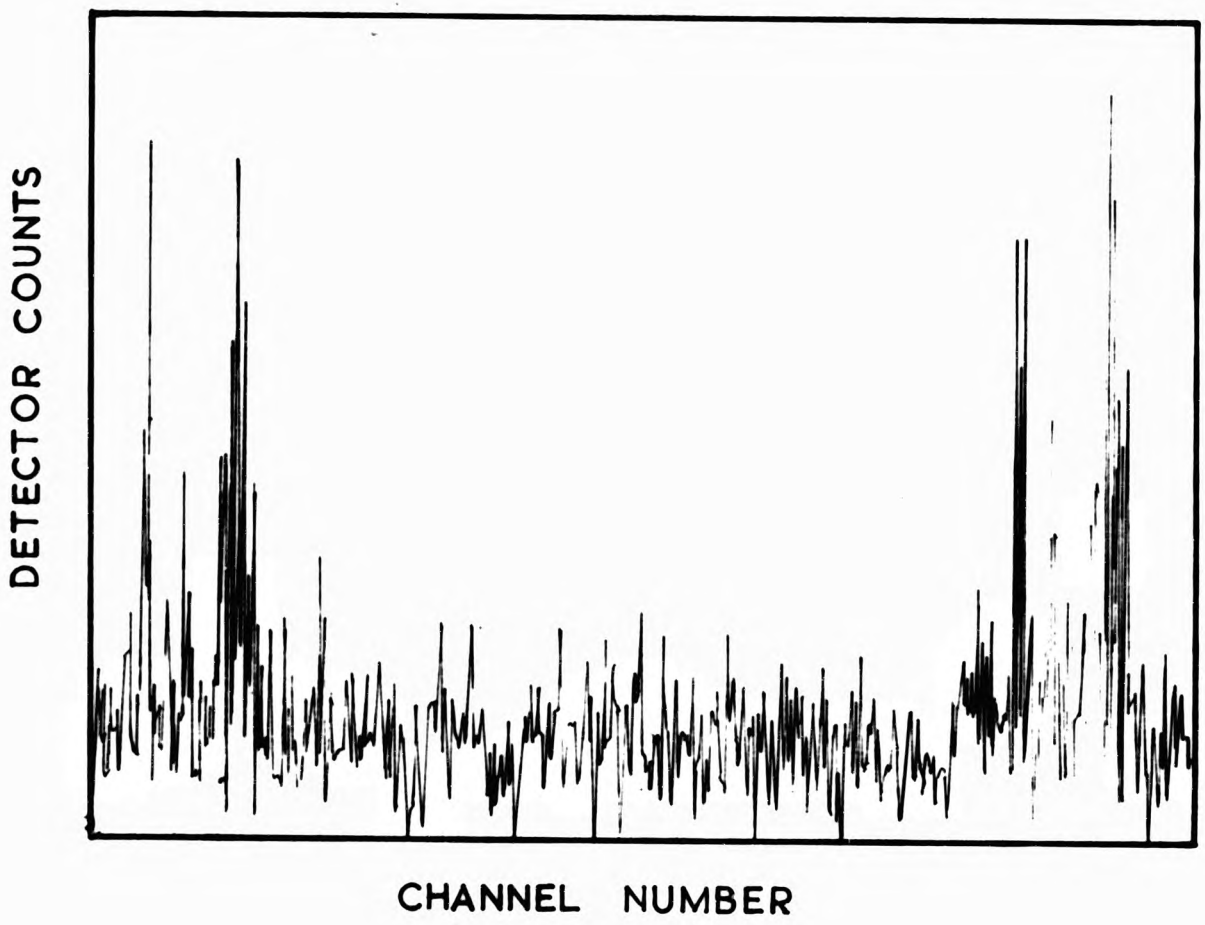

Figure 5.3(a)

^{54}Mn k-emission spectrum from ^{55}Fe electron capture (EC) x-ray source as recorded by the crystal x-ray spectrometer using Nacℓ(100) crystal.

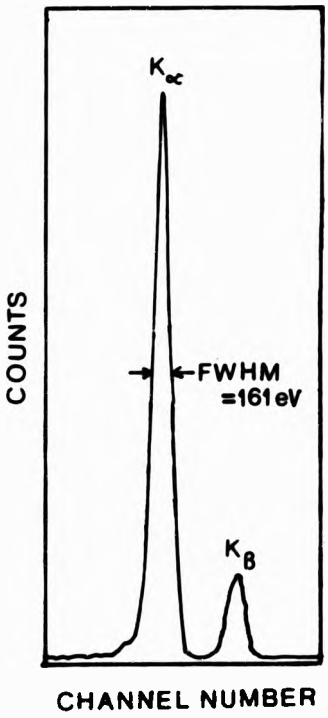

Figure 5.3(b): ^{54}Mn K_{α} and K_{β} line spectrum as recorded by the HPGe detector.

CHAPTER 6

CONCLUSION

6. CONCLUSION

The electron-ion coincidence studies of the electron-atom collision process have provided new data of partial double-differential cross sections, DDCS(n+), for the ionization of helium, argon, krypton and xenon atoms under electron impact. While the present DDCS(n+) data for argon agrees with the previous experimental data, there seems to be no such data available for comparison for the atoms of helium, krypton and xenon. The presently found relative values of DDCS(n+) and DDCS are shown in section 5.1 as a function of the detected electron energy (between 25 eV to 300 eV) and as a function of the incident electron energy (0.5 keV to 10 keV).

In the detected electron energy region where the energy of the ejected electron corresponds to that of an Auger electron the values of DDCS(n+) represent mainly the cross section values for the inner-shell responsible for that Auger electron emission. For argon atoms, for example, when the energy of the detected electron equals that of an LMM Auger electron the presently found charge distribution of argon ions agrees well with the calculated values of Hippler et al. (1984b). Thus DDCS(n+) values for the Auger electron energy region provide useful information about inner-shell ionization.

The present DDCS ($= \sum_n$ DDCS(n+) values for helium are found to agree generally with the experimental data of Opal et al. (1972) and the theoretical values of Bell and Kingston (1975). The present DDCS values for argon, krypton and xenon have also been compared with the experimental values of Opal et al. (1972) at incident electron energy of 500 eV as there is no data available in literature for comparison at higher incident electron energies.

The results of x-ray-ion coincidence experiment show that highly charged xenon ions are associated with the emitted x-rays indicating that multiple

ionization results from the vacancy cascades following the emission of x-rays by the xenon ion which has a vacancy in the inner-shell. The presently found charge distribution of xenon ions detected in coincidence with the emitted x-rays agrees well with that found by photoionization of inner-shells.

The present experimental data gives an insight into the process of multiple ionization and can not only be useful for testing the existing theoretical models but also can help in the formulation of a theory which can give a fuller explanation for the process of multiple ionization.

It is suggested that the variation of DDCS(n+) with the angle of ejection of the detected electron may also be investigated to obtain further useful information about the collision process.

In the present x-ray-ion coincidence experiment it was not possible to separate the effect of different characteristic x-ray lines emitted by the xenon ion. This can perhaps be achieved in future with the help of the crystal x-ray spectrometer as it has not only a higher energy resolution but can also separate the x-ray lines spatially, making it possible to select any x-ray line for the x-ray-ion coincidence experiment.

The crystal x-ray spectrometer can also, in future, be applied for a better x-ray spectroscopy of the characteristic x-ray lines emitted by the ion and it can also be used to study the polarization of the x-ray lines.

It is also suggested that triple coincidence experiments (coincidences between the scattered electron, the ejected electron and the ion) may be carried out in future to obtain further precise information about the electron-atom collision process.

APPENDIX

Computer programme for controlling the crystal x-ray spectrometer.

```
REM . . PROGRAMME TO CONTROL STEPPING MOTOR AND MCA . ..
IN = 65120 : OUT = 65120 : DR = 65122
?DR = 255
REM ..... NO. OF SCANNING REPETITIONS DESIRED ......
INPUT "NO. OF SCANS", R
REM ..... TOTAL NO. OF STEPS OR CHANNELS TO BE SCANNED ......
INPUT "NO. OF STEPS", N
REM ..... TIME PER CHANNEL IN SECONDS......
INPUT "TIME BET. STEPS", T
IF R = 0 THEN END
REM .... TO PUT THE MCA IN COLLECTION MODE ....
?OUT = 4
?OUT = 0
?OUT = 4
FOR  K = 1 TO R
REM ..... PRINT STATEMENT TO INDICATE THE NO. OF THE SCANNING BEING
   DONE ......
PRINT "MOTOR FORWARD K" ; K
FOR I = 1 TO N
PRINT "NO. OF STEP I" ; I
REM .... TO MOVE THE STEPPING MOTOR ONE STEP FORWARD ....
?OUT = 5
?OUT = 15
? OUT = 5
REM .... TO MAKE THE SPECTROMETER WAIT FOR THE TIME SPECIFIED
   AS T SECONDS ......
TIME = 0
IF TIME < 100*T THEN GO TO
REM .... TO REPEAT SPECIFIED STEPS N ....
```

```
NEXT I
REM ... TO PUT THE MCA OUT OF COLLECT MODE AT THE END OF SCANNING ....
?OUT = 4
?OUT = 0
?OUT = 4
REM .... STEPPING MOTOR MOVES THE CRYSTAL TO ORIGINAL POSITION ....
PRINT "MOTOR BACK"
FOR J = 1 TO N
PRINT "J = " ; J
?OUT = 4
?OUT = 6
?OUT = 4
TIME = 0
IF TIME < 100 THEN GO TO
NEXT J
REM .... TO REPEAT THE SCANNING ....
NEXT K
REM .... AT THE END OF THE SPECIFIED SCANNING ....
GO TO (Beginning of the programme).
END
```

REFERENCES

Åberg T., in: Atomic Inner-shell Processes, Vol.1, p353, (ed. B. Craseman), Academic Press, 1975.

Afrosimov V.V., in: Proceedings of the second Int.Conf. on Inner-shell ionization phenomenon (ed. W. Mehlhorn & R.Brenn), University Freiburg, 1976, p258.

Arthurs A.M. and Moiseiwitsch B.L., (1958), Proc.Roy.Soc.A247, 550.

Auger P., 1925, J. de Phys. et le Radium 6, 205.

Balashov V.V., Lipovetsky and Sanshenko V.S., (1973) Sov.Phys.JETP 36,858.

Beckman, O. (1955). Ark.Fys. 9, 495.

Bell K.L. and Kingston A.E., (1975), J.Phys.B8, 2666.

Bethe H., 1933, In "Handbuch der Physik" (S.Flugge, ed.), Vol.24.1, Springer Verlag, Berlin.

Bethe H., 1930, Ann.Phys., 5, 325.

Beyer H.F., Hippler R., Schartner K.-H., and Albat R., Z.Phys.A 289 239 (1979); 292, 353 (1979).

Birks L.S. in: 'X-ray Spectroscopy' (H.K. Herglotz and and L.S. Birks Ed.) Dakkar, New York (1978).

Boehm F., 1975, in: Atomic inner-shell processes, edited by Craseman B., (Academic, New York) p411.

Bonsen T.F.M. and Vriens L., (1970) Physica 47, 307.

Borchert G.L., Hansen P.G., Johnson B., Lindgren I., Ravon H.L., Shult O.W.B. and Tidemand-Peterson, (1978) Phys.Letts 65A, 297 and 66A, 347.

Borchert G.L., Hansen P.G., Johnson B., Ravon H.L., Shult, O.W.B. and Tidemand-Peterson, 1977, Phys.Lett. 63A, 15.

Bransden B.H. and McDowell M.R.C., 1969, J.Phys.B., 2, 1187.

Bransden B.H. and McDowell M.R.C., 1970, J.Phys.B., 3, 29.

Burhop E.H.S., 1940, Proc. Camb. Philos. Soc. 36, 43.

Burhop E.H.S. (Cambridge 1952), The Auger effect and other radiationless transitions.

Cairns R.B., Harrison H. and Shoen R.I., (1969), Phys.Rev. 183, 52.

Campbell J.L., (1968), Nucl. Instrum. Methods 65, 333.

Carlson T.A. and Krause M.O., 1965, Phys.Rev.137A, 1655.

Carlson T.A. and Krause M.O., 1966, Phys.Rev.151, 41.

Carlson T.A. and Nester Jr. C.W., 1973, Phys.Rev. A8, 2887.

Chaudhry M.A., Duncan A.J., Hippler R. and Kleinpoppen H., (1986), Abstracts of Tenth Int. Conf. on Atomic Physics, Tokyo, Japan, (August 1986) p391.

Chen M.H., Craseman B., Yin L.I., Tsang T., Adler I., Phys.Rev.A13, 1435 (1976).

Chen M.H., Crasemann B., Aoyagi M., Huang K-N. and Mark H., 1981, At. Data Nucl. Data Tables 26, 561.

Coghlan W.A. and Clansing R.E., 1973, At.Data 5, 317.

Cooper J.W. and Kolbenstvedt H., Phys.Rev. A5, 1972, 677.

Culhane J.L. and Fabian A.C., (1972), IEEE Trans.Nucl.Sci.NS-19, 569.

Culhane J.L., Herring J., Sandford P.W., O'Shea G. and Phillips R.D. (1966), J.Sci.Instrum. 43, 908.

De Heer F.J. and Jansen R.H.J., 1977, J.Phys.B., 10, 3741.

De Heer F.J., Jansen R.H.J. and van der Kaay W., 1979, J.Phys.B12, 979

Diethorn W., 1956, Thesis, Carnegie Inst. Technol. Pittsburg, Pennsylvania, U.S.A.

Dyson N.A. (1959), Brit.J.Appl.Phys.10, 505.

Dyson N.A., X-rays in Atomic and Nuclear Physics (Longman, London, 1973).

Eggarter E., 1975, J.Chem.Phys. 62, 833.

Egorov A.I., Radionov A.A., Ryl'nikov A.S., Sovestrov A.E., Sumbaev O I. and Shaburov V.A., 1978, JETP. Lett.27, 483.

Ehrhardt H., Hesselbacher, K.H., Jung K., Willmann K. (1972). In Case Studies in Atomic Collision Physics II (McDaniel E W., McDowell M.R.C., eds.) 161-210, Amsterdam, North-Holland Publishing Company.

Fano U., (1963) Ann.Rev.Nucl.Sci. 13, 1.

Fano U., 1935, Nuovo Cimento 12, 156.

Fink R.W., in: Atomic Inner-shell Processes II, ed. Craseman B; (Academic Press, New York, London, 1975).

Franklin J.L., Heirl P.M. and Whan A., 1967, J.Chem.Phys. 47, 3148.

Gibson D.K. and Reid I.D., 1986, J.Phys.B. 19, 3265.

Glassgold A.E. and Ialongo G., 1968, Phys.Rev. 175, 151.

Glassgold A.E. and Ialongo G., 1969, 186, 266.

Gold R and Bennet E.F., 1966, Phys.Rev.147, 201.

Green T.S. and Proca G.A. (1970) Rev.Sci.Instrum., 41, 1409.

Hansen P G., Johnson B., Borchert G.L. and Schult O.W.B., in Atomic Inner-shell Physics, ed. B. Craseman, (Plenum, New York, 1985), p.237.

Harbach T., 1980, Dipl. Thesis, Fault&t für Physik, Universit&t Bielefeld, West Germany.

Hatch E.N., 1964, Z.Physik 177, 337.

Hippler R. and Jitschin W., 1982, Z.Phys.A.307, 287.

Hippler R., Bossler J. and Lutz H.O., 1984a, J.Phys.B 17, 245.

Hippler R., Saeed K., Duncan A.J. and Kleinpoppen H., 1984b, Phys.Rev.A30, 5.

Hippler R. in Progress in Atomic Spectroscopy (Part C) eds. Beyer H.J. and Kleinpoppen H. (Plenum Press, New York and London), 1984c.

Inokuti M., Kim Y.K. and Platzmann R.L., 1967, Phys.Rev.164, 55.

Inokuti M., 1971, Rev.Mod.Phys. 43, 297.

Isozumi Y. and Isozumi S. (1971), Nucl. Instrum. Methods 96, 317.

Jacobowicz H. and Moores D.L., In: Electron-atom and Electron-molecule Collisions, Juergen Hinze ed., Plenum Press, New York (1983).

Jenkins R. and De Vries J.L. (MacMilland 1970), Practical X-ray Spectroscopy.

Jitschin W., Wisotzki B., Werner U. and Lutz H.O., (1984), J.Phys.E: Sci.Instrum.17 137.

Kieffer L.J. and Dunn G.H., 1966, Rev.Mod.Phys., 38, 1.

Kim Y-K. (1983), Phys.Rev.A, 28, 656.

Kim Y.-K. and Inokuti M., 1973, Phys.Rev.A7, 1257.

Kopfermann H., 1958, Kernmomente (Academic, New York).

Krause M.O. in: Photoionization and Other Probes of Many-Electron Interactions, p.133 (ed. F Wuilleumier) Plenum Press, 1976.

Krause M.O., 1979, J.Chem.Phys. Ref. Data 8, 307.

Kuyatt C.E., 1968, in: 'Methods of Experimental Physics' (L. Marton, ed.) Vol.7A, p1, Academic Press, New York.

Laundau L.D. and Lifshitz E.M., Quantum mechanics non-relativistic theory (Pergamon Press Ltd. 1965) p.579.

Lee P.L. and Boehm F., 1973, Phys.Rev.C8, 819.

Lewyn L.L., 1970, Nucl. Instrum. Methods 82, 138.

Lucas C.B., 1973, J.Phys.E. 6, 991.

Luyken B.F.J., De Heer F.J. and Baas R.Ch. (1972), Physica 61, 200.

Madison and Shelton, W.N. (1973), Phys.Rev.A7, 499.

Manson S.T., Tuburen L.H., Madison D.H. and Stolterfoht N.(1975) Phys.Rev.A12,6(

Massey H.S.W., Burhop E.H.S. and Gilbody H.B., 1969, 'Electronic and Ionic Impact Phenomenon', 2nd ed. Clarendon Press, Oxford.

Massey H.S.W. and Mohr C.B.O.: Proc.Roy.Soc. A140 (1933) 613.

McGuire E.J., (1974) Phys.Rev. A9, 1840.

McGuire J.H., 1982, Phys.Rev.Lett. 49, 1153.

Mehlhorn W. in: Photoionization and other probes of many-electron interactions, p309 (Ed. F Wuilleumier) Plenum Press, 1976.

Mehlhorn W., 1968, Z. Phys. 208, 1.

Mehlhorn W., 1978, 'Electron Spectroscopy of Auger and Autoionization States. (Lecture notes). Fakultat fur Physik, Universitat Freiburg, Germany

Mokler P.H., Folkmann F., in: Structure and Collisions of Ions and Atoms, ed. Sellin I.A., (Springer Verlag, Berlin, 1978) p201.

Moores D., Golden L.B., Sampson P., 1980, J.Phys.B13, 385.

Morita S., 1983, Research Report, Institute of Plasma Physics, Nagoya University, Nagoya, Japan.

Mott N.F. and Massey H.S.W.: The theory of atomic collisions, 3rd ed. (Oxford at the Clarendon Press 1965) p489.

Nagy P., Skutlartz A. and Schmidt V., 1980, J.Phys.B13, 1249.

Oda N., Nishimura F. and Tahira S., 1972, J.Phys.Soc.Japan 33, 462.

Ogurtsov, G. N., 1973, Sov.Phys. JETP 37, 584.

Oldham Jr. W.J.B., 1965, Phys.Rev. 140A, 1477.

Oldham Jr. W.J.B., 1967, Phys.Rev. 161A, 1.

Oona H., 1974, Phys.Rev.Lett. 32, 571.

Opal C.B., Peterson W.K. and Beaty E.C., 1971, J.Chem.Phys.55, 4100.

Opal C.B., Peterson W.K. and Beaty E.C., 1972, Atomic Data 4, 209.

Perlman H.S., 1960, Proc.Roy.Soc.(London) 76, 623.

Peterkop R., 1977, "Theory of Ionization of Atoms by Electron Impact" Colorado Associated University Press.

Peterson W.K., Opal C.B. and Beaty E.C., 1971, J.Phys.B4, 1020.

Peterson W.K., Opal C.B. and Beaty E.C., 1972, Phys.Rev.A5, 71.

Proca G.A. and Green T.S., 1970, Rev.Sci.Instrum. 41, 1778.

Ravon J.P., 1982, Nucl.Instrum. & Meth. 211, 7.

Rosseland S., 1923, Z.Phys. 14, 172.

Rudd M.E., Sautter C.A. and Bailey C.L., Phys.Rev. 151 (1966) 20.

Rudge M.R.H., 1968, Rev.Mod.Phys. 40, 564.

Sandstrom A.E., 1957, in Handbuck der Physik, edited by Fugge S. (Springer Verlag, Berlin) p.78.

Saxon R.P., 1973, Phys.Rev.A8, 839.

Schnopper H.W. (1960), Physical Rev. 154, 118.

Schmitz W. and Mehlhorn W., 1972, J.Phys. E5, 64.

Schram B.L., 1966, Physica, 32, 197.

Segre E., (Wiley 1953-59) Vol.III, Experimental Nuclear Physics.

Shergin A.P. and Gordeev Yu S. in: Invited Papers and Progress Reports of X Int.Conf. on the Physics of Electronic and Atomic Collisions, Paris, 1977, p.377.

Short R.T., C.-S.O., Levin J.C., Sellin I.A., Liljiby L., Huldt S., Johansson S.-E., Nilsson E. and Church D.A., 1986, Phys.Rev.Lett.56, 2614.

Shyn T.W. and Sharp W.E., 1979, Phys.Rev.A.19, 557.

Shyn T.W., Sharp W.E. and Kim Y.-K., 1981, Phys.Rev.A24, 79.

Sneddon I.N., Fourier Transforms (McGraw Hill, 1951) p.365.

Stolterfoht N., de Heer F.J. and Van Eck J., 1973, Phys.Rev.Lett.30, 1159.

Sumbaev O.I., and Merzentsev A.F., Sov.Phys.JETP 21, (1965) 295.

Sumbaev O.I., 1976, Chemical Effects in X-ray Spectroscopy in Modern Physics and Chemistry (Academic, London) Vol.1, p.31.

Sumbaev O.I., 1970, Sov.Phys.JETP 30, 927.

Tahira S. and Oda N., 1973, J.Phys.Soc.Japan 35, 582; Proc. of the 8th Int. Conference on the Physics of Electronic and Atomic Collisions, Belgrade, 1973, pp.443-63.

Van der Wiel M.J. and Wiebes G., 1971, Physica 53, 225.

Vriens L., Case studies in atomic collision physics I, eds. E.W. McDaniel and M.R.C. McDowell (North Holland Publishing Co. Amsterdam 1969) Ch.6.

Vriens L., Physica 47 (1970), 267.

Vriens L., 1969, Case Studies in Atomic Collision Physics, eds. E.W. McDaniel and M.R.C. McDowell (North Holland Publ. Co., Amsterdam) V2.

Vroom D.A., Palmer R.L. and McGowan J. Wm., (1977), J.Chem.Phys.66, 647.

Wendin G. and Ohno M., (1976), Physica Scripta 14, 148.

Wentzel G., 1927, Z.Phys. 43, 524.

Werner U., 1983, Dipl. Thesis, Fakultät für Physik, Universität Bielefeld, West Germany.

Wetzel W.W., 1933, Phys.Rev. 44, 25.

Wille U. and Hippler R., 1986, Physics Reports 132, 3 and 4.

Worthington C.R. and Tomlin S.G. (1956), Proc.Phys.Soc.A69, 401.

Yin L.I., Adler I., Tsang T., Chen M.H., Ringers D. and Craseman B: Phys.Rev.A9, 1070 (1974).

Younger S.M., (1985): In Electron Impact Ionization (Mark T.D. and Dunn G.H., eds.) Springer-Verlag Wien, New York.